JGR Solid Earth

RESEARCH ARTICLE

10.1029/2022JB023997

Key Points:

- A method developed for distributed strain measurements in high-confinement triaxial tests using fiber optics sensing
- The method has been tested for up to 200 MPa of confining pressure using granite, gabbro, and sandstone samples
- The development of evolving strain localization that corresponds to a fault-like rupture was observed in all triaxial tests

Correspondence to:

A. Salazar Vásquez,
antonsal@student.ethz.ch

Citation:

Salazar Vásquez, A., Rabaiotti, C., Germanovich, L. N., & Puzrin, A. M. (2022). Distributed fiber optics measurements of rock deformation and failure in triaxial tests. *Journal of Geophysical Research: Solid Earth*, *127*, e2022JB023997. https://doi.org/10.1029/2022JB023997

Received 11 JAN 2022
Accepted 20 JUL 2022

Author Contributions:

Conceptualization: Antonio Salazar Vásquez, Carlo Rabaiotti, Leonid N. Germanovich, Alexander M. Puzrin
Formal analysis: Antonio Salazar Vásquez, Leonid N. Germanovich
Funding acquisition: Carlo Rabaiotti
Investigation: Antonio Salazar Vásquez
Methodology: Antonio Salazar Vásquez, Carlo Rabaiotti, Leonid N. Germanovich
Project Administration: Carlo Rabaiotti, Alexander M. Puzrin
Supervision: Carlo Rabaiotti, Leonid N. Germanovich, Alexander M. Puzrin
Validation: Antonio Salazar Vásquez
Visualization: Antonio Salazar Vásquez
Writing – original draft: Antonio Salazar Vásquez, Leonid N. Germanovich

Distributed Fiber Optics Measurements of Rock Deformation and Failure in Triaxial Tests

Antonio Salazar Vásquez[1,2], Carlo Rabaiotti[2], Leonid N. Germanovich[3], and Alexander M. Puzrin[1]

[1]ETH Zurich, Zurich, Switzerland, [2]Eastern Switzerland University of Applied Sciences, Rapperswil, Switzerland, [3]Clemson University, Clemson, SC, USA

Abstract The implementation of distributed strain measurement methods in triaxial and uniaxial tests have demonstrated the development of strain localization, even at early stages. This implies that single point measurement methods are location dependent. The use of distributed methods is required not only to improve the interpreted constitutive parameters obtained from triaxial tests, but also to understand the implications of strain localization in the failure process. This work uses optical fibers in triaxial tests. The developed distributed measurement method was implemented on granite, gabbro, and sandstone samples and tested under different confining pressures, reaching 200 MPa on the granite sample. Using a temporal resolution of 0.25 Hz and 5 mm of spatial resolution, the strain evolution at over 300 locations at the sample surface was measured during testing. When compared to point sensing methods, the use of optical fiber greatly increases the number of measurements at the surface of the sample, and their interpolation provides the entire deformation of the sample surface. In all the tests performed, strain localizations were revealed before failure. A three-dimensional interpretation of a test, combining an optical scan of the sample and the distributed measurements, show good correlation between the fractures and the strain localization.

Plain Language Summary Triaxial tests are commonly used to describe the response of rock materials under loading and to predict their failure. The sample is assumed to develop a uniform deformation; therefore, single point sensors are used. The recent implementation of computer tomography scans and acoustic emission techniques in triaxial tests have shown the evolution of strain localization prior to failure. This implies that distributed measurement methods are required to improve interpretation of the material behavior and understand its failure mechanisms. This work uses optical fibers in triaxial tests. The developed distributed strain measurement method was compared to widely accepted point measurement methods. It was then used in rock samples, capturing the distributed deformation on their surfaces with higher temporal resolution than the computer tomography scanning method. In all the tests performed, strain localizations were revealed, evolving through the height of the sample. A three-dimensional reproduction, combining an optical scan and the distributed measurements, show good correlation between the fractures and the strain localization.

1. Introduction

Constitutive models are used to describe the mechanical behavior of materials (Karev et al., 2020; Nadai, 1963; Puzrin, 2012). These consist of mathematical equations that can be used to relate physical quantities and are defined by material-specific constants (Davis & Selvadurai, 2005). The design of civil engineering structures relies on the precise calibration of these constants (Alonso et al., 2010; Puzrin et al., 2010). Triaxial tests are commonly carried out to obtain the constitutive parameters of geomaterials (Jaeger et al., 2007). It is generally assumed that the triaxial test is a representative volume test, meaning that the developed stresses and strains are uniform in the sample. Accurate detection of a sample's strain is important for the determination of the mechanical properties. Linear variable differential transformers (LVDT) and strain gauges are common technologies to measure the strain response. The drawback is that the measurement is limited to the point or small zone where they are installed, forcing the assumption of a homogeneous sample response in accordance with the representative volume assumption. However, recent numerical and experimental studies have shown strain localization in the samples, even at early test stages (McBeck et al., 2019; Van der Baan & Chorney, 2019). This implies that when point measurement methods are used, the mechanical parameters obtained are dependent on the sensor location.

Writing – review & editing: Carlo Rabaiotti, Leonid N. Germanovich, Alexander M. Puzrin

The use of distributed measurement methods can provide the strain field over the entire surface of the sample, solving the point measurement location dependency. In addition, their application in laboratory tests has shown promising advances in the investigation of other physical phenomena. Van der Baan and Chorney (2019) implemented a numerical model of a triaxial test using the bonded-particle method, showing the development of heterogeneous force networks within the sample. They concluded that the intensity of the stress heterogeneity is related to the seismicity that originated during the failure process. McBeck et al. (2019) measured the distributed strain in a triaxial test using the computer tomography (CT) scanning method. They observed localization of contractive strain preceding dilatation and shear localization. These strain localizations preceded the macroscopic yielding of the sample and coincided with its dilatation. Higo et al. (2013) implemented two distributed methods to measure strain in a low confinement triaxial test; microfocus X-ray CT and digital image correlation. The measured displacement field showed that localized shear deformation developed before the shear bands became visible. These studies have exposed the complexity of the failure process, even in highly controlled environments. As the use of distributed measurement methods becomes widespread, more data will become available to study the correlation between strain localization with seismicity and fracturing, which might provide a better understanding of the failure process (Bernard, 2001; Bohnhoff et al., 2016; Cornet et al., 1998; Durand et al., 2021; Martínez-Garzón et al., 2021; Scotti & Cornet, 1994). Even though X-ray and CT scanning has been successfully applied to measure distributed strain in triaxial tests, the major disadvantage is the long measurement time (2 hr per measurement registered by Higo et al., 2013), which can cause interruptions to the test procedure. Additionally, the required equipment is large, complex, and expensive, making this technology incompatible with most triaxial systems.

When compared to CT scanning, fiber optics technology has the ability to measure the distributed strain with a much higher sampling rate (minutes and often hours for the CT and only seconds for the optical fiber interrogator). Additionally, its implementation into existing triaxial systems is less complex because it requires only a millimetre diameter fiber inside the triaxial cell and, hence, one channel to measure the distributed strain over the entire fiber length. Similar to other methods, optical fiber technology does not measure strain inside the sample. In contrast to CT scanning, the fiber must be coupled with the sample; therefore, attention must be given to the installation, glue, and fiber selection. Figure 1 shows the two principal components: the interrogator and the optical fiber. In the experimental setup, the optical backscatter reflectometer (OBR 4600) was used. The OBR is based on Rayleigh scattering, and, in our opinion, is the most suitable for laboratory applications because of its high spatial resolution (~1 mm) and its sampling rate (~0.25 Hz). Further details on the technology are given in Appendix A. The technology has been introduced in diverse civil engineering applications, due to its reliability, precision, and high spatial resolution (Crameri et al., 2019; Hauswirth, 2015; Hauswirth et al., 2014; Inaudi & Glisic, 2005; Minardo et al., 2012; Moffat et al., 2015; Rabaiotti & Malecki, 2018; Vorster et al., 2006; Xu et al., 2016).

Fiber bragg grating (FBG) is a point strain measurement method that uses similar single mode fibers as the OBR technology (Domingues & Ayman, 2017). The implementation of several FBGs in the same fiber can act as a quasi-distributed method. The main advantage of FBG is that it measures with a kHz sampling rate. FBG has been implemented in uniaxial and triaxial tests, proving the feasibility of using single mode fibers for measuring strain on rock and concrete samples at unconfined and confined conditions (Kovalyshen et al., 2018; Schmidt-Hattenberger et al., 2003; Sun et al., 2016; Yabesh et al., 2021; Yang et al., 2007).

Recently, Sieńko et al. (2019) and Uchida et al. (2015) used the OBR to measure distributed strain in uniaxial compression tests on acrylic and concrete samples, respectively. Uchida et al. (2015) positioned the optical fiber in a helicoid configuration to capture the entire superficial strain field, showing that even artificial homogeneous isotropic samples suffer non-uniform deformation. Sieńko et al. (2019) observed strain localization, which they attributed to crack development within the concrete surface, showing the potential of the method to study failure. In the present study, the use of the fiber optics technology to measure distributed strain is extend to high confining pressure triaxial tests (up to 200 MPa). The distributed method was first developed (Section 2) using a steel sample implemented with optical fiber and strain gauge sensors. Later, in Section 3, the method was tested on Central Aare granite, Zimbabwe gabbro, and gray, and green Bernese sandstone, assessing the distributed method for

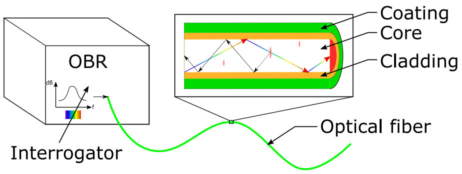

Figure 1. Components of fiber optics distributed measurement method.

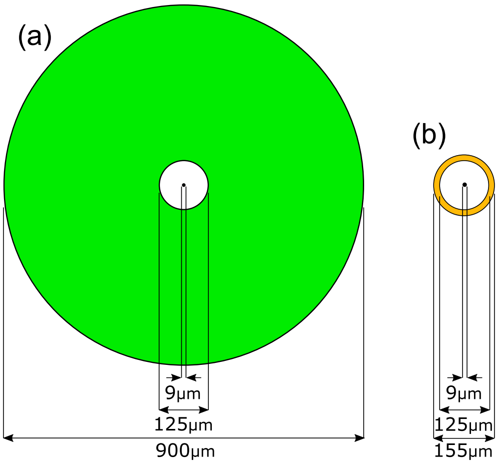

Figure 2. Schematic cross-sections of the optical fibers. (a) 900 μm acrylate-coated fiber manufactured by Solifos AG. (b) 155 μm polyimide-coated fiber manufactured by Fibercore.

a wide range of strength (40–270 MPa) and stiffness (4–103 GPa). The measured distributed strain was superimposed on a light scan of a failed sample, showing that the strain localization correlated with the position where fractures appeared on the surface.

2. Development of the Distributed Strain Measurement Method

The present section aims to test the applicability of the method using simple uniaxial tests, assess the performance of the selected combination of the fiber and glue (adhesive), and develop an optimal fiber layout for later use in triaxial tests. For this purpose, the results of a simple uniaxial test on a homogeneous steel sample are shown and discussed. The sample was implemented with strain gauges and fiber optics to compare the measurements.

2.1. Equipment and Sensors

Optical fibers developed for sensing and telecommunication are composed of an inner cylindrical core surrounded by two layers: cladding and coating (Figure 1). While the cladding ensures that the light beam (pulse) is confined within the core, the coating improves the mechanical properties, protecting the fiber from physical damage. Two single mode fibers were selected for this work: 900 μm diameter acrylate-coated and 155 μm diameter polyimide-coated (Figure 2). The strain coefficient was calibrated prior to the test, being $C_\varepsilon = 150$ for the poliyimide fiber and 149 for the acrylate fiber. The fibers were chosen by considering two effects: light attenuation and strain lag. Light attenuation caused by micro-bending can lead to light loss and, consequently, make measurement impossible. Several authors have shown that the fibre's coating alters the strain transfer between the medium and the core (strain lag), and they developed numerical and theoretical models to correct the measurements (Alj et al., 2020; Ansari & Libo, 1998; Bassil et al., 2020; Billon et al., 2015; Falcetelli et al., 2020; Tan et al., 2021; Wang & Zhou, 2014; Wang et al., 2016; Wang & Xiang, 2016; C. Zhang, Shi, et al., 2020; S. Zhang, Liu, et al., 2020). The results in this work are not corrected by any strain lag model for three reasons: (a) Strain lag models have been developed for known strain fields, while the strain fields in triaxial tests are complex and unknown (McBeck et al., 2019). (b) Theoretical strain lag models have assumptions that are not met in the triaxial system (Wang & Zhou, 2014). (c) Most of the models were developed for field applications with fiber/cables, which are considerably thicker than the selected fibers (Figure 2). For example, the theoretical strain lag proposed by Zheng et al. (2021) for the polyimide-coated fiber is 0.5 cm, while for the acrylate-coated fiber it is 1.1 cm, which is considerably smaller compared to other fibers. The OBR technology is sensitive to confining pressure and temperature changes (Appendix A). Nevertheless, no pressure or temperature compensation was considered because the uniaxial test was carried out under constant confining pressure and temperature.

The OBR 4600 interrogator manufactured by Luna Innovations (https://lunainc.com/) was used in the present work. The device has a high strain resolution (micro strain $\mu\varepsilon = 10^{-6}$) and millimetre spatial resolution that are sufficient for laboratory tests on relatively small samples. The interrogator has a sampling rate of 0.25 Hz but only one optical channel; therefore, each fiber was interrogated every 8 s with the use of an optical switch. A test typically lasted 30–60 min. Appendix A describes the methodology and the adopted post-processing procedure.

The tests were carried out in a triaxial system that generates confining pressures up to 200 MPa, using oil to conduct pressure. The triaxial cell can accommodate cylindrical samples with a maximum diameter of 7 and 14 cm height. Further details are given in Appendix B.

2.2. Uniaxial Test Setup

The uniaxial tests were performed on a cylindrical steel sample, instrumented with the optical fibers (Figure 2) and strain gauges. The comparison between technologies applied in a simple test allowed for assessing the distributed method and for studying the fiber's strain lag. A slightly off-centered axial load was applied to induce a

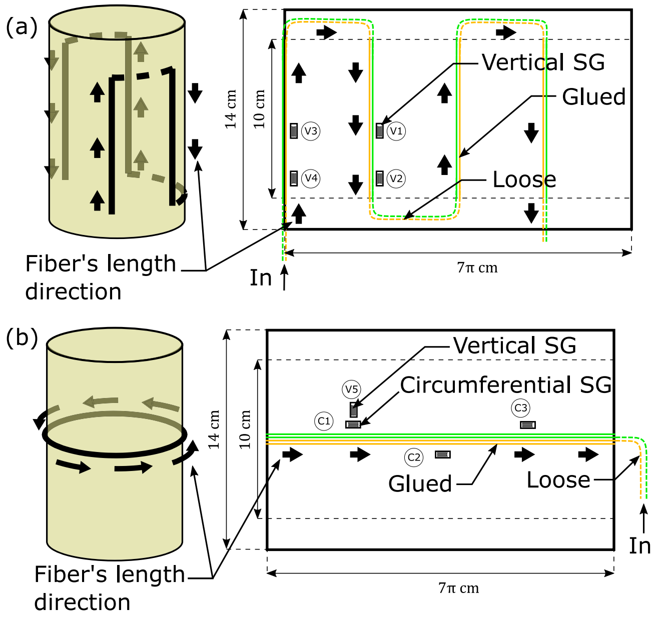

Figure 3. Uniaxial test layouts implemented with the acrylate- (green) and polyimide-coated (yellow) optical fibers. The continuous lines represent where the fibers are glued to the sample, while dashed lines are loose fiber sections. The strain gauges measuring grid size are 4.5 mm long and 3.2 mm wide (SGD-5/350-LY11 manufactured by Omega Engineering, https://www.omega.com/en-us/). (a) The axial layout comprises four lines parallel to the axial load, equally distanced on the perimeter and four axial (vertical) strain gauges (V1, V2, V3, and V4). (b) The circumferential layout comprises two fully glued circumferential loops at the middle of the sample and three strain gauges attached in the circumferential direction (C1, C2, and C3). One strain gauge was implemented in the axial direction (V5).

non-uniform strain field, enhancing the advantages of the distributed measurements. The fibers were placed in position using pre-tension and fixed with a cold-curing instant adhesive. A two part epoxy was used to cover the fibers, to protect them during test preparation and to improve the strain transfer (from the sides of the fibers).

Two configurations were assessed to measure the expected principal strains: the maximum strain (ε_1) in the axial direction (Figure 3a) and the minimum strain (ε_3) in the circumferential direction (Figure 3b). In the axial direction a compressive strain is expected, while tensile strain is expected in the circumferential direction. In each configuration the measurements are one-dimentional (along the fiber), but when implemented together they result in a two-dimensional distributed surface measurement. Separate testing of axial and circumferential configurations and their comparison to the strain gauge measurements enabled the capability of the method under different deformation mechanism to be assessed. In our setup, the triaxial cell has four strain gauge feed-through ports, restricting the number of optical fiber segments that can be implemented because the objective is to compare both technologies. Since the metal sample is not broken during testing, we have the advantage of testing these configurations separately, and, due to the limitation of the number of strain gauge feedthroughs, the axial and circumferential configurations were tested in two different tests. In the tests on rock samples described in Section 3, both the axial (Figure 3a) and circumferential (Figure 3b) configurations were implemented simultaneously.

In the axial configuration, four equidistant vertical lines were instrumented. The strain gauges were glued parallel to the corresponding first vertical lines, two at the beginning of the lines (V2 and V4) and two in the middle of the sample (V1 and V3). Each pair allowed the strain development distance of the fibers to be studied. The circumferential configuration consisted of two loops surrounding the middle of the sample. Three strain gauges (C1, C2, and C3) were glued adjacent to the fibers in the circumferential direction. One vertical strain gauge (V5) was attached to verify the Poisson's ratio. The distribution of the strain gauges in the circumferential configuration prioritizes studying the capability of the optical fiber to measure the non-uniform strain field. The outputted distributed data has two columns: the fiber distance to each "distributed" gauge and the strain measured at this position. To spatially reference the data on the sample, several locations (gauges) were identified: closest positions to the strain gauges, end-begging of axial lines and crossing of the circumferential fiber with some pre-draw lines. To locate the gauges, the fiber was point heated with a 5 mm diameter steel rod, allowing referencing the distributed data on the sample. The uncertainty in the gauge identification is the selected gauge length for data post-processing and does not exceed ±5 mm. This uncertainty is the same for all measurement locations.

2.3. Results of the Method Development

The distributed measurements obtained with the acrylate and polyimide fibers are compared in Figure 4. Each continuous gray-scaled line is a distributed measurement at diverse differential loads over the length of the fiber, following the sample's schematics below each figure. The strain gauge positions are marked with colored dashed lines. The distributed axial strain measured with the polyimide fiber is shown in Figure 4a, while 4b details the measurements from the acrylate fiber. The same comparison for the circumferential direction is given in Figures 4c and 4d, where the "sinusoidal" distribution reflects the non-uniformity of the strain field caused, as mentioned in Section 2.2, by applying the axial load slightly off-center to the sample. When comparing the axial measurements obtained with the polyimide and the acrylate fibers (Figures 4a and 4b), it can be seen that the second fiber registered lower values at the beginning and end of each vertical line (round edges in Figure 4b). Towards the middle of the sample both fibers measured similar values, reflecting the higher strain lag due to the thicker coating. For example, the difference at the V4 position is 13.7%, while at V1 the differences is 4.02%. This effect is considerably diminished in the circumferential direction (Figure 4c), mainly due the increase of the

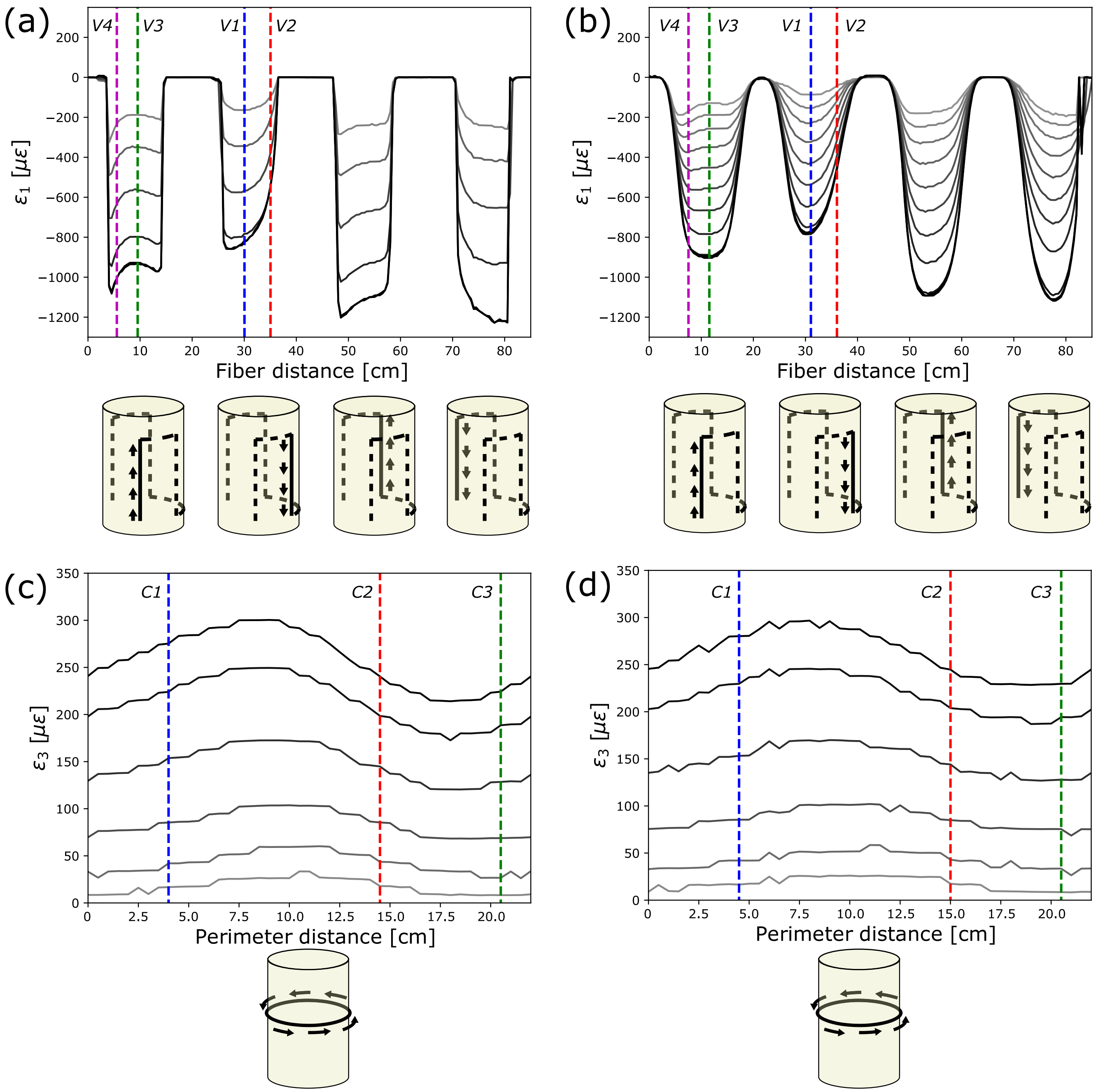

Figure 4. Axial (ε_1) and radial (ε_3) distributed strain measurements. Solid lines denote distributed strain at different times and correspond to different differential loads ($q = \sigma_1 - \sigma_3$), while dashed lines mark the strain gauge positions. (a) Polyimide fiber measurements in the axial configuration (Figure 3a). (b) Acrylate fiber measurements in the axial configuration (Figure 3a). (c) Polyimide fiber measurements in the circumferential configuration (Figure 3b). (d) Acrylate fiber measurements in the circumferential configuration (Figure 3b). The strain gauge positions are marked by vertical lines with notation shown in Figure 3.

frictional force inherent to this orientation. Nevertheless, a slight difference can be seen at the highest and lowest values (at 8 and 17.5 cm along the perimeter), where the acrylate fiber tends to the average (~1% difference at 8 cm).

In order to compare the distributed and point measurement methods, Figure 5 shows the strain at the same positions plotted against the differential stress. To take into account the location uncertainty in the distributed data (±5 mm as discussed above), the average of three fiber optics gauges (closest to a strain gauge and its nearest neighbors) is plotted in Figure 5. Since we are comparing fiber optics and strain gauge measurements

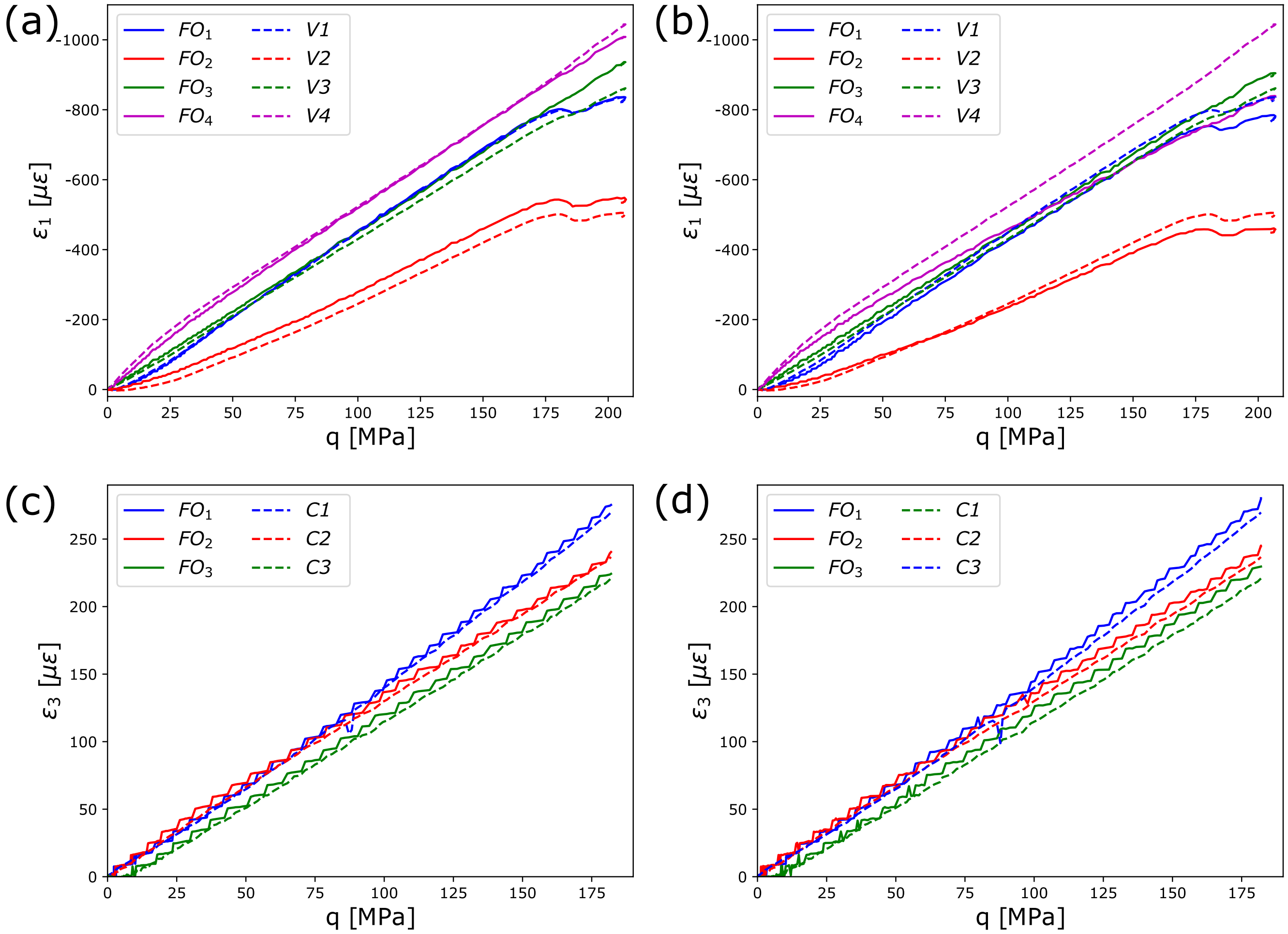

Figure 5. Comparison between distributed (solid lines) and point (dashed lines) measurement methods. Optical fiber (FO) measurements are shown at the strain gauge positions. To take into account an uncertainty in locating the FO gauge positions, the FO measurements are averaged over located positions of the FO gauges (closest to strain gauges) and their nearest preceding and following neighbors. On all plots, $q = \sigma_1 – \sigma_3$, $\mu\varepsilon = 10^{-6}$. Letters "V" and "C" indicate vertical (axial) and circumferential strain gauges, respectively. (a) Axial configuration measured with the polyimide fiber. (b) Axial configuration measured with the acrylate fiber. (c) Circumferential configuration measured with the polyimide fiber. (d) Circumferential configuration measured with the acrylate fiber. See Figure 4 caption for more details.

from almost the same locations (with 5 mm accuracy), the loading conditions do not significantly influence the comparison. Strain gauges located at the ends of the implemented vertical lines (V2 and V4) recorded higher values than the acrylate fiber (Figure 5b. 13.9% difference compared to V4), but were similar to the polyimide fiber (Figure 5a. 0.228% difference compared to V4). In the middle of the sample both fibers are in accordance with the strain gauge data (5% difference for the acrylate fiber and 0.54% for the polyimide fiber). This indicates that the distance required by the acrylate fiber to develop the strain is greater than 1 cm and less than 4 cm, while for the polyimide fiber it is only a few millimetres. Both results are in agreement with the theoretical strain lag distance calculated using the method proposed by Zheng et al. (2021); 1.2 cm for the acrylate-coated and 0.5 cm for the polyimide-coated fiber. In the circumferential direction, the acrylate fiber measurements, on average, have a 3% difference to the strain gauge data. In contrast, the difference for the polyimide fiber reduced to 1.5% (Figures 5c and 5d). In other words, the measurements obtained using the polyimide-coated fiber are reliable for both orientations (axial and circumferential) and through the entire glued segments. In the circumferential direction, the distributed data obtained with the acrylate-coated fiber is also reliable, but its implementation in the axial direction (compressive deformation) requires consideration of the strain lag. For the sample size used in this work (14 cm) the reliability is limited to the central section of the fiber.

In non-uniform strain fields, point measurement methods are insufficient and distributed methods are required. This is shown in Figure 6, where the advantages of the distributed strain measurements are enhanced. The axial

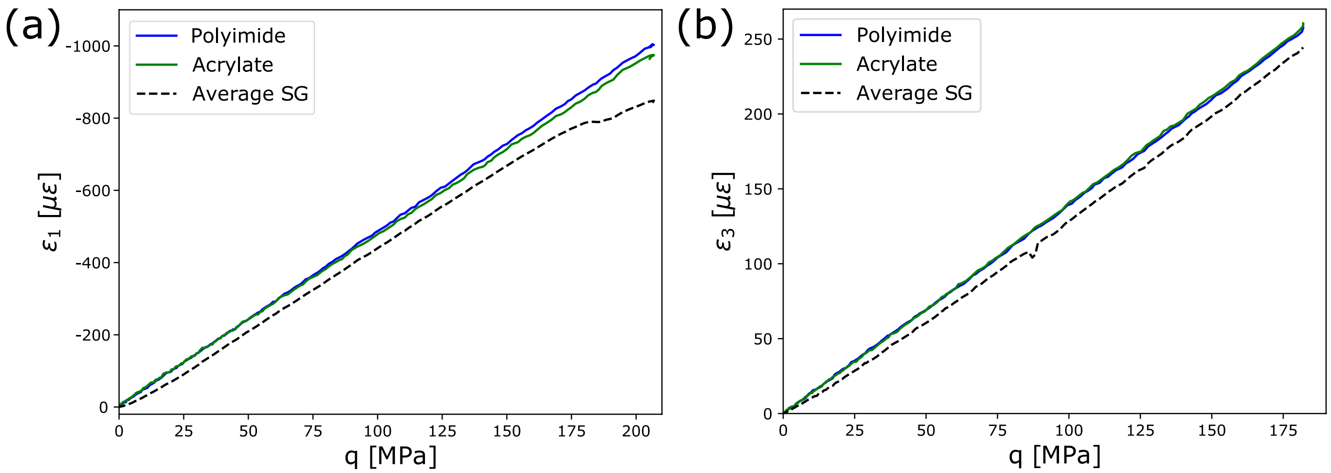

Figure 6. A comparison of the measured strain average between distributed and point measurement methods ($q = \sigma_1 – \sigma_3$, $\mu\varepsilon = 10^{-6}$). (a) The vertical strain (ε_1) is the average of the four points on the vertical fiber near the middle of the sample. It is compared to the average strain from the axial strain gauges, V1 and V3 (Figure 3a). (b) Average of the distributed circumferential strain (ε_3) compared with the average of the circumferential (horizontal) strain gauges, C1, C2, and C3 (Figure 3b).

strain measured in the middle of the sample is averaged for the strain gauge and distributed technologies and is shown in Figure 6a. When considering only the central values in the axial direction (stretch not affected by strain lag) both cables perform similarly, with a difference of 2% between them. A non-linear behavior is seen in the strain gauge data at about $q = 175$ MPa (Figures 5 and 6). This was due to a rotation on the sphere that applies the load, between the sample and the piston. The rotation probably contributed to the strain field non-uniformity described above. This non-linearity, however, does not change the average of the distributed data, because the measurements covered a much greater surface of the sample. Figure 6b contrasts the average of the circumferential distributed strain and the average measurements from the corresponding strain gauges (C1, C2, and C3). The difference in the circumferential average measured with the optical fibers is approximately 1%, while the strain gauges registered a value 5.5% lower. This is explained by the fact that the strain gauges were installed on the less loaded side of the sample, highlighting their location dependency. This is evidenced in Figure 4, where the strain gauge positions coincide with the zone where lower strain was measured with the distributed method.

Even though the polyimide-coated fiber is more accurate, the use of the acrylate fiber is not discarded. In Appendix C, the results of isotropic confinement tests are given, indicating light attenuation problems caused by micro-bending. Polyimide-coated fibers on a polished steel surface were able to measure the distributed strain under confining pressures up to 80 MPa. If applied to rock surfaces, attenuation problems are apparent at 15 MPa. Fiber crossing can also produce light attenuation. Small voids at the sides of the overlapped fiber allows the overlapping fiber to bend when confining pressure is applied. Additionally, at this pressure range, the stretches of the fibers that are loose in the oil show a linear spectral shift with confinement, indicating the pressure sensitivity of the technology (Appendix C). This information cannot be used to compensate for test measurements in which the confining pressure is not constant. To obtain the compensation factor, tests with fibres glued on materials with known properties are necessary. In this work, no compensation is required because all measurements were taken at constant pressure and temperature. This is described in more detail in Section 3 and Appendix C.

3. Distributed Strain Measurement Method in Triaxial Tests

The previously developed distributed measurement method was used on rock samples and tested under confined and unconfined conditions. The complexity of the results presentation gradually increases in this section, from conventional point measurement to virtual reproductions of the sample. The goal is to show that the distributed strain measurement method can be implemented to not only obtain traditional data, but also to provide further understanding of the failure process.

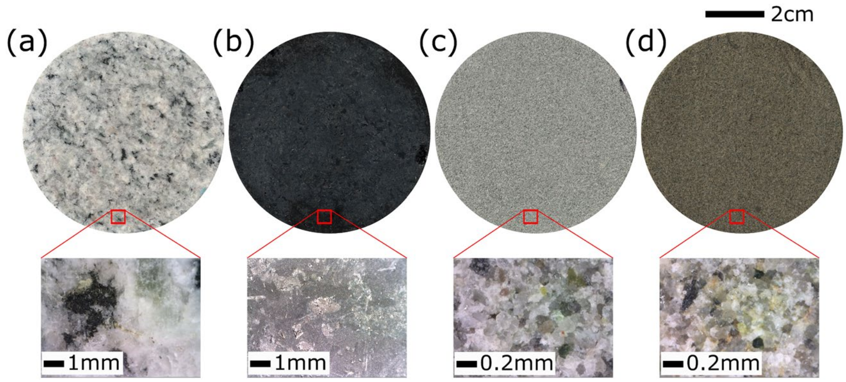

Figure 7. Lithologies at two different scales. (a) Central Aare granite samples collected from Wassen in Switzerland. (b) Zimbabwe gabbro of unspecified location. (c) Gray Bernese sandstone collected from Bern city center. (d) Green Bernese sandstone collected from Bern city center.

3.1. Sample Preparation

Cylindrical samples, 7 cm in diameter and 14 cm in height, were cored from four different lithologies: Central Aare granite (Switzerland), gabbro (Zimbabwe), gray and green Bernese sandstone (Switzerland; Figure 7). The Central Aare granite (Figure 7a) is a medium biotite grained granite with a recognizable magmatic structure, dominated by quartz, potassium feldspar and greenish colored plagioclase (Labhart et al., 2015). The biotite inclusions are evenly distributed in the sample, with an irregular shape of about 2.7 mm long. The Zimbabwe gabbro is composed by plagioclase, mica, biotite and amphibole quartz (Figure 7b). Inclusions are homogeneously distributed and the samples have isotropic mechanical properties (Liu, 2021). Bernese sandstone has a homogenous fine grained lithology composed of quartz, calcite, feldspar, and mica (Kellerhals et al., 2005; Materials Hub, 2017). Samples of green and gray Bernese sandstone were tested, but blue and yellow tones can also be found, depending on the degree of glauconite oxidation (Kündig et al., 1997). The grains of the gray Bernese sandstone have an approximate diameter of 0.15 mm (Figure 7c), while the grain diameter of the green Bernese sandstone is 0.2 mm (Figure 7d). The reported porosity of the Bernese sandstone is 0.24–0.27 (Materials Hub, 2017). Porosity of the intact granite and gabbro samples does not exceed 1%. This lithology selection incorporates a wide range of rock stiffness and strength.

The granite and sandstone samples were instrumented with the acrylate-coated fiber to avoid micro-bending, due to the high confining pressure used on the granite and the rough sandstone surface. Polyimide fiber was selected for the gabbro samples, because of its smoother surface and lower confining pressure. An estimation of the sandstone roughness can be made from their mean grain size, which is ~0.2 mm. Figure 8 shows the optical fiber configurations used, differing only in the axial optical fibers (vertical lines) included in configuration b. Granite and gray Bernese sandstone samples were instrumented with configuration (b), while gabbro and green Bernese sandstone were implemented with configuration (a). All samples were prepared, jacketed and tested in

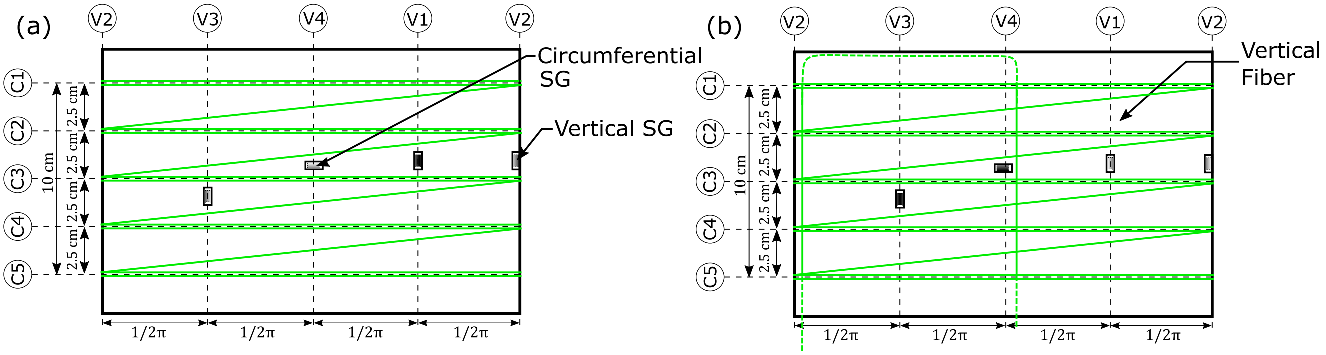

Figure 8. Optical fiber configuration used in the triaxial tests. (a) Configuration composed of five circumferential optical fiber loops at different levels and four strain gauges (SG). (b) Configuration composed of two axial optical fiber stretches, five optical fiber loops in the circumferential direction and four strain gauges.

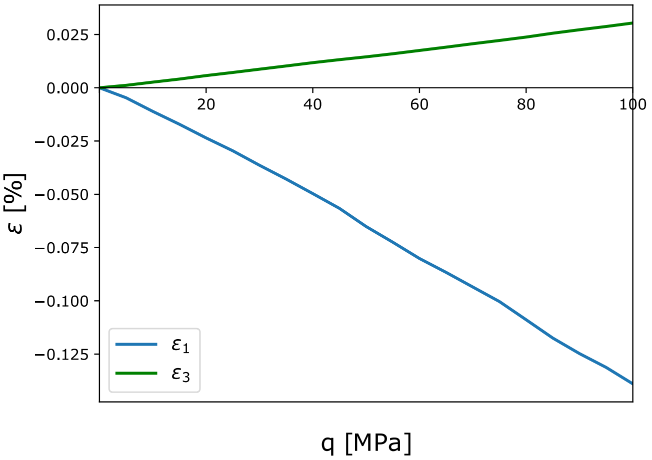

Figure 9. Differential stress ($q = \sigma_1 – \sigma_3$) versus strain response of the Central Aare granite tested at 200 MPa confinement. The axial (ε_1) and circumferential (ε_3) strain are from selected locations of the distributed measurements.

the laboratory environment (temperature ~20°C, pressure ~1 bar and humidity ~76%). The samples were first isotropically confined, and then an incremental and uniform (centered) axial displacement was imposed at a constant rate of 9.91 $\mu\varepsilon/s$.

Appendix A describes the OBR measuring method and the post-processing sequence used to obtain the distributed strain. The method calculates the strain variation between two measurements and is sensitive to temperature, strain and pressure (Appendix C). Since measurements were taken at constant pressure (after confinement), and, therefore, constant strain coefficient, no pressure compensation was considered necessary. The confinement increases the temperature of the oil, with an expected ~1°C variation during differential loading due to heat dissipation. In a loose section of the cable (i.e., between the sample and the feed-through port), where temperature and temperature-deformation effects occur, this temperature variation induces a spectral shift of 1.24 GHz, which is equivalent to ~8 $\mu\varepsilon$. The equivalent strain is lower when considering the temperature coefficient of a cable restricted to deformation (only temperature effects). This strain represents less than 1% of the expected maximum strain, therefor no temperature compensation was needed.

Similar to the uniaxial tests (Section 2.2), the positions of interest in the distributed data were identified by touching the fiber with a heated steel rod with an accuracy of 1 mm. This procedure allows the identification of the beginning and end of the circumferential and axial lines, mapping all the distributed information on the sample.

3.2. Point Method Results

Data obtained with point methods are usually restricted to line graphs and assume that the sample behaves homogeneously. One such common presentation is the stress versus strain response, which is shown in Figure 9 for a Central Aare granite sample tested at 200 MPa confining pressure. The plotted strain data is from selected single points of the distributed measurements (both axial and circumferential) located at the middle of the sample. The calculated Young's modulus at the elastic stage is 72 GPa, and the Poisson's ratio is 0.22. These values are consistent with other experiments on samples with similar lithologies. For example, Li et al. (1999) measured a Young's modulus of 69.9 GPa and Poisson's ratio of 0.27 on Bukit Timah granite tested at 170 MPa confining pressure. These values are within the ranges of 13–85 GPa and 0.14–0.34 given by Domede et al. (2019) for Young's modulus and Poisson's ratio, respectively, for 178 different granites (albeit at different confining pressures).

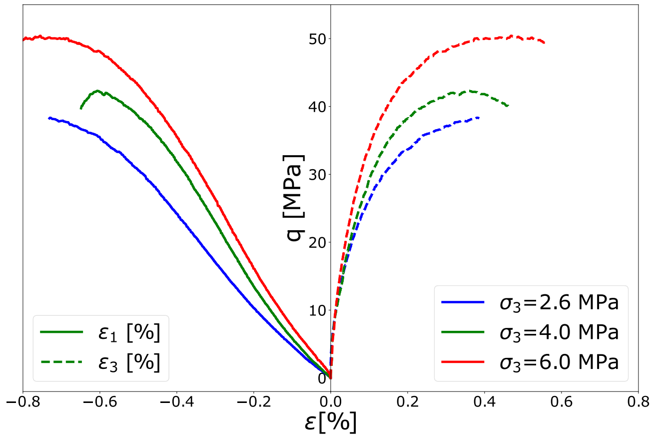

Figure 10. Strain versus stress response of the gray Bernese sandstone at different confining pressures. The vertical strain (ε_1) is the average of the two points on the vertical fiber near the middle of the sample, while the circumferential strain (ε_3) is the average of all the distributed circumferential data.

The results from three gray Bernese sandstone samples tested at confining pressures of 2.6, 4, and 6 MPa are shown in Figures 10 and 11. The samples were loaded until failure, but the stress drops and post-failure behavior are not shown because the macro fracture (rupture) that split the sample also damaged the fibers, rending further measurements impossible. The circumferential strain in Figure 10 is the average of the distributed measurement of all circumferential segments. The axial strain is the average of the two measurements taken at the positions crossing the middle of the sample. As expected (e.g., Jaeger et al., 2007), the sandstone exhibits an increase in non-linearity and stiffness with confinement (Figure 10). Nevertheless, the low maximum strain developed before failure (<0.8%) indicates that the material behavior is brittle.

The principal strain data was adopted to compute the volumetric ($\varepsilon_v = \varepsilon_1 + 2\varepsilon_3$) and the shear strains ($\varepsilon_s = (\varepsilon_1 - \varepsilon_3)2/3$) in Figure 11. The first advantage of the distributed method can be seen by comparing the volumetric behavior calculated from the entire sample (average of lines C1, C2, C4, and C5 in Figure 8b) to the response at the middle (average of line C3). A larger

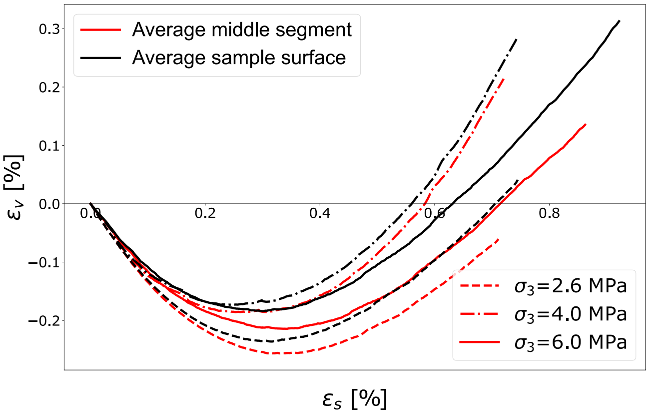

Figure 11. Gray Bernese sandstone samples tested under confined conditions. Volumetric strain ($\varepsilon_v = \varepsilon_1 + 2\varepsilon_3$) plotted against shear strain ($\varepsilon_s = (\varepsilon_1 - \varepsilon_3)2/3$). The volumetric response is compared for the distributed data from the entire sample surface versus the middle segment.

volumetric strain was observed at the ends of the sample (top and bottom) compared to the middle; this difference increases with confinement for these tests. The material initially reduces its volume, followed by a significant dilatation. This response can explain the hardening at small loads and the softening toward failure, as shown in Figure 10.

3.3. Distributed Strain Measurement Method Results

The circumferential strain evolution of a Zimbabwe gabbro sample is shown in Figure 12a. The distributed measurements of each circumferential level given in Figure 8a are plotted with different colors, and their intensity reflects the imposed axial load increment. The horizontal axis is the distance along the perimeter of the sample from an arbitrary axial line (unwraped surface). The color code of each level of the distributed data follows the scheme in the legend of Figure 12b. In a homogeneous sample, the distributed strain should be constant (horizontal lines), increasing with load. At low loads (lighter colors), the distributed strain is relatively homogeneous, but close to failure (darker colors) strain starts developing faster at 5 cm in the perimeter (indicated with arrows), especially at lower stress levels (at about 80% of the maximum load). The strain localization started at level C4, and propagated towards levels C5 and C3. Figure 12b gives a comparison of single points (gauges) of the distributed data that have the highest (red dashed line) and the lowest (blue dashed line) strain, together with the levels' average (following the same color code). At the position of the minimum strain (Section 1), the behavior remains linear until 90% of the maximum stress, while the maximum strain (Section 2) initiates an exponential growth from 50% of the maximum stress. Level C1 average shows a slightly lower strain response than the others, but all indicate non-linear behavior starting at about 80% of the maximum load. The results from a second gabbro sample tested at 10 MPa confinement are given in Appendix D. A strain localization that propagated in the sample towards the end of the tests was also observed.

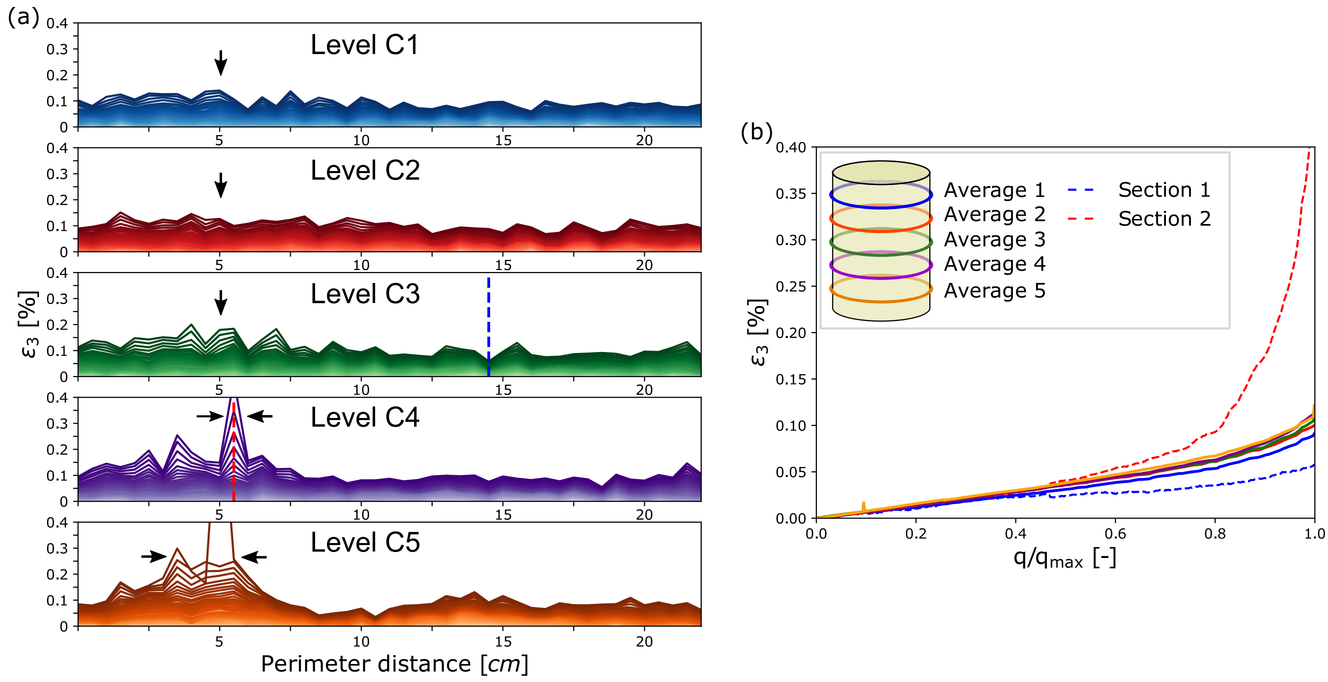

Figure 12. Zimbabwe gabbro tested under unconfined (uniaxial) conditions. (a) Circumferential distributed strain measurements at each of the levels (Figure 8b). Color intensity marks the loading increment, being darker for higher loads. The positions of the maximum and minimum strains are marked with red and blue dashed lines, respectively. (b) Circumferential strain development with normalized differential stress ($q = \sigma_1 - \sigma_3$). The average for each level is compared with the maximum and minimum strain in the sample.

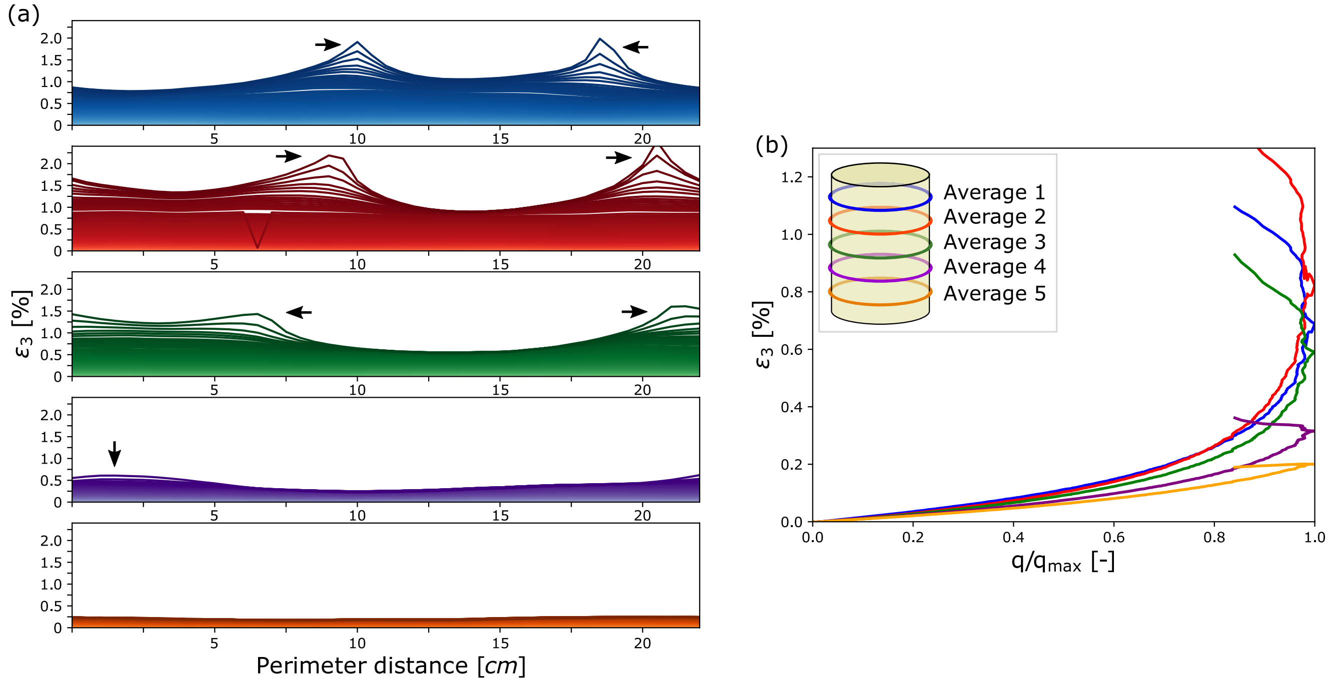

Figure 13. Green Bernese sandstone tested under 16 MPa confinement. (a) Circumferential distributed strain measurements at each of the levels (Figure 8b). Color intensity marks the loading increment, being darker for higher loads. (b) Average strain development per level. Circumferential strain development with normalized differential stress ($q = \sigma_1 - \sigma_3$). The average of each level is compared.

The test performed on green Bernese sandstone at 16 MPa confining pressure shows the greatest differences within the sample's levels (Figure 13a). The maximum measured strain at level C5 is about 0.2%, while it is ten times higher at level C2. Two clear strain localizations developed in levels C1, C2, and C3 (indicated with arrows). In level C2, a single localization is visible at the projection of upper level localizations. Figure 13b reveals that, from the early stages, the upper side of the sample develops higher strain (levels C1 and C2); from 40% of the maximal load, the difference increases exponentially and is close to linear behavior at level C5, while it is exponential in level C2.

The distributed measurement method allows for an extension of the results to show the material behavior in detail. The last measurement of the test performed on the green Bernese sandstone (Figure 13a) was interpolated to obtain the strain on the sample surface, as shown in Figure 14. The angle formed by the strain concentrations is more evident in this plot. This information was used to superimpose the strain on a 3D scan of the sample taken after the test (Figure 15). The sample was placed on a rotating table and scanned using the Space Spider light scanner (https://www.artec3d.com/), with a sub-millimetre precision. Axial lines drawn prior to the test were used to reference the coordinate system of the scan. The distributed data was superimposed on the virtual sample using the same orientation: no additional rotation or adjustment was done. Failure was driven by a macro fracture, dividing the sample in two: The upper part is shown in Figure 15b, while the lower in Figure 15c. The virtual reproduction in Figure 15a shows that the strain localization at the upper levels (C1, C2, and C3) correlates with the position where the fracture manifests on the surface. Figures 15b and 15c indicate the fault's dip direction to vertical at about levels C4 and C5. This change in direction was followed by a sudden fracture propagation that caused sample failure. The strain localization is not obvious on the fracture's position at levels C4 and C5, because the fracture propagation speed, after the change in direction, exceeded the OBR interrogator's time resolution.

An additional test on green Bernese sandstone is presented in Appendix D. At unconfined conditions the macro fracture-driven failure was sub-vertical, which was also reflected in the distributed measurements. An assessment of the accuracy of the distributed method under confinement conditions is given in Appendix E.

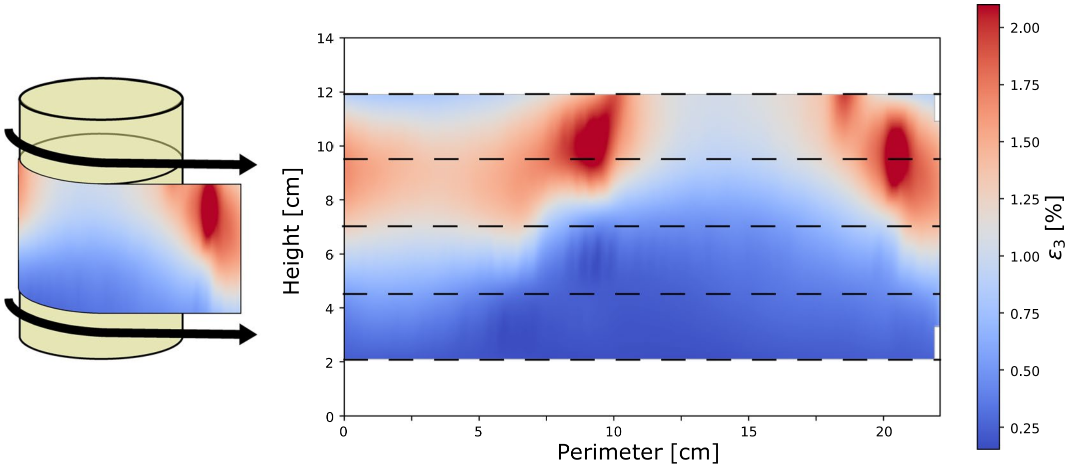

Figure 14. Circumferential strain field on sample's surface (green Bernese sandstone). The data from the last distributed measurement of Figure 13a was interpolated. Black dashed lines indicate the locations where the distributed strain was measured.

4. Discussion

Uniaxial tests were carried out to assess the reliability of the distributed method. Additionally, Figure E1 gives a comparison between the strain gauge and a single location of the distributed measurements under confined conditions and at large strain (~1%). The correct selection of optical fiber is critical for the application of the current method in triaxial tests. The cable stiffness, which depends on the coating material and its thickness, is important to ensure the quality of the strain data collected by the fiber senors (e.g., strain transfer and light attenuation). Under low confining pressures (<15 MPa) or unconfined tests, the thinner (or stiffer) coated fibers are recommended for measuring the distributed circumferential and axial strain. To avoid light attenuation, thicker (or softer) coatings should be used under high confinement or when the sample surface is rough (e.g., sandstone). The correct implementation also requires consideration of the height of the sample. For example, the acrylate fiber used in the present research should not be used for samples shorter than 10 cm because of the strain lag. For short samples, a combination of distributed and point methods can be implemented: the optical fiber to measure the distributed circumferential strain and strain gauges in the axial direction (e.g., configuration shown in Figure 8a). In the circumferential direction, the average of the distributed strain is reliable for both fibers. When compared to strain gauges, the distributed circumferential data showed a 3% difference using the acrylate-coated fiber and 1.5% when using the polyimide-coated fiber. Two different fibers can also be used to avoid bending at fiber crossings. A thin fiber should be glued in the axial direction, with a thicker fiber overlapping to measure the circumferential strain. The thinner fiber at the bottom reduces the voids on the side of it, where the overlapping fiber can bend due the confining pressure. In any event, the effects of fiber crossing and fibers pressing on one another are too small and do not show up in the distributed data (Figures 12a, 13a, D1a and D2a). The distributed method can potentially be extended to high temperature conditions. The polyimide fiber used in this research is rated up to 300°C, and temperature resistant acrylate-coated fibers are industrially available (e.g., SM1500 HT manufactured by Fibercore can withstand up to 150°C). Besides coating stiffness, other physical and chemical interactions of the coating with the host media should be considered. For example, some polymer and acrylate coatings swell in contact with water, and the swelling depends on salt concentration, PH, and presence of other chemical substances (Bai & Seitz, 1994; Janting et al., 2019; Khanikar & Singh, 2021; McCurley & Seitz, 1991; Sedighi et al., 2021; Shakhsher et al., 1994).

In all tests performed, strain localizations were seen at multiple heights. The probable cause is fracture nucleation inside the sample and its subsequent propagation (Bobet, 2000; Germanovich et al., 1994; Katz & Reches, 2004; Reches & Lockner, 1994). The first observation supporting this hypothesis is the correlation between the localizations and the location where the fracture manifests on the surface of the sample (Figure 15a). Additionally, sub-vertical fractures were observed in samples tested with low confinement, which is in accordance with the measured localization distribution (Figures 12, D1 and D2).

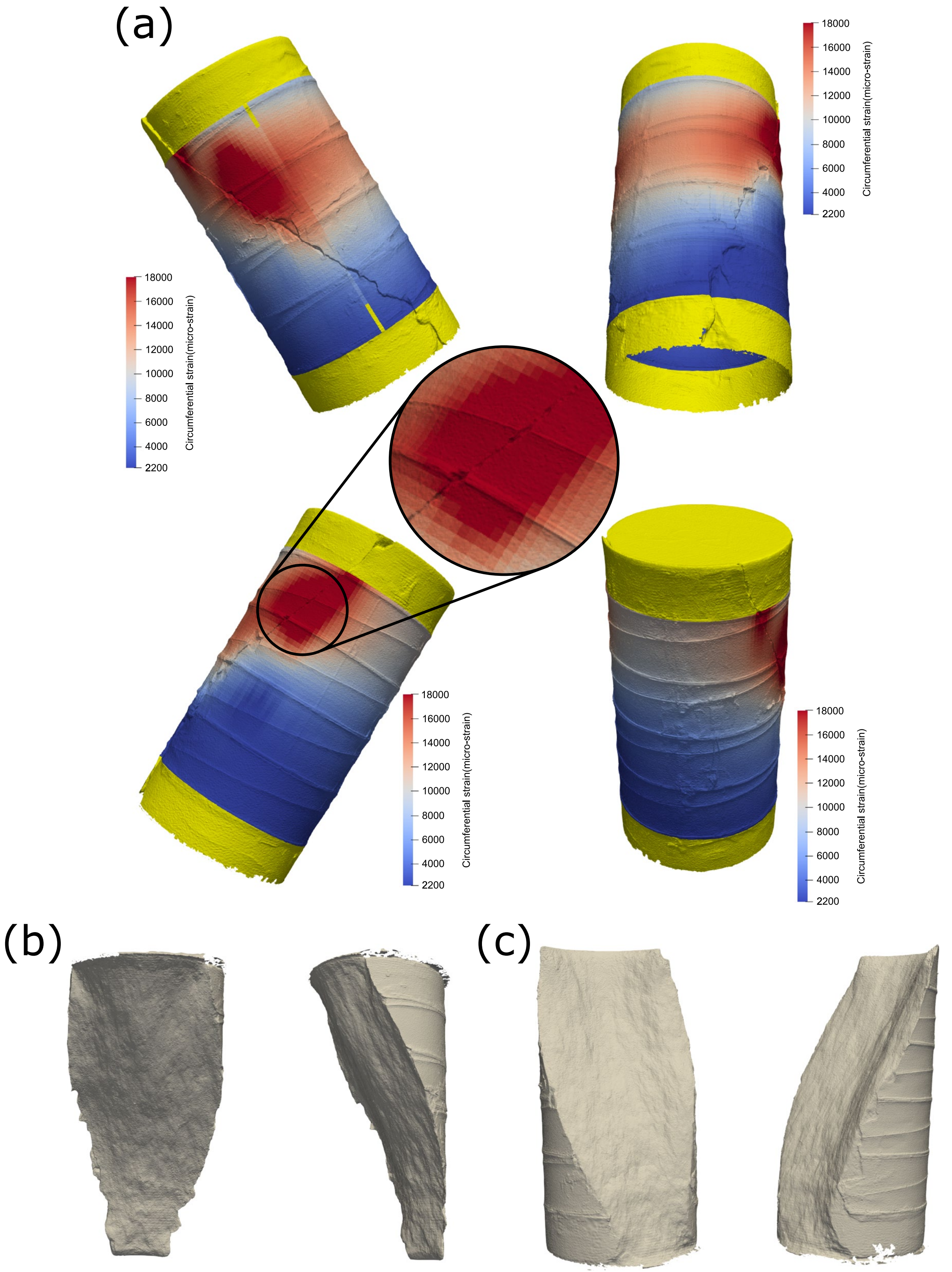

Figure 15. 3D optical scan post failure, which was caused by a macro fracture dividing the sample in two of the green Bernese sandstone. (a) The scan is colored with the interpolated circumferential strain from Figure 14. (b) Upper part of the sample after failure. (c) Lower section of the sample after failure. The dip direction of the fracture surface experienced a verticalization at level C4 and C5.

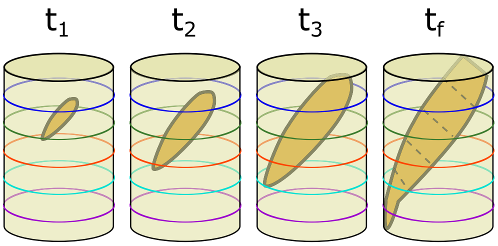

Figure 16. Probable internal fracture nucleation and propagation. Arbitrary time stamps during the test are denoted by t_i, time is until failure t_f ($t_1 < t_2 < t_3 < t_f$). Dashed lines in the last time stamp indicate the intersection of the fracture with the horizontal plane where the circumferential optical fibers were implemented.

Our intepretation of the failure process in the green Bernese sandstone sample tested under 16 MPa (Figure 13) is outlined in Figure 16. At the early stages (t_1), the fracture nucleates closer to the top (between levels C1 and C2). This discontinuity (rupture) grows in a stable manner towards the bottom and the side surface (t_2 and t_3). This would explain the higher average strain of level C1 and C2 at low loads, followed by level C3 (Figure 13b). Towards failure the strain localization becomes more pronounced, because the fracture is approaching the side surface of the sample (Figure 13a). Finally, the fracture becomes unstable and changes the propagation direction downwards (t_f), splitting the sample.

The interpretation of internal fracture propagation (Figure 16) could also explain the difference between the volumetric response averaged over the middle segment and entire sample surface (Figure 11). In most of the performed tests (Figures 12a, 13a, D1a and D2a), the largest signals were registered at approximately one radius from the sample ends, propagating towards the middle. We explain this observation by the nucleation and propagation of a macro fracture. Tests at larger confining pressure result in a more inclined macro-fracture. An inclined fracture leads to more fracture presence in one end of the sample than in the middle. This can be observed in Figure 16, where the fracture area, projected into the upper horizontal cross-section (upper dashed lines in Figure 16), is greater than in the middle of the sample (middle dashed line). This may explain the lower volumetric strain measured in the middle of the samples, while the increasing inclination explains the increasing volumetric difference between the middle and the sample average with confining pressure.

In triaxial tests, fractures in the samples show several recognized patterns (e.g., Jaeger et al., 2007). For example, the fracture may show an X-type pattern under confining pressure. Based on this hypothesis, the optimal fiber layout schemes on the surface of the sample can be designed to monitor potential fracture propagation and to reduce the number of trials and errors.

An important question is whether the rupture schemed in Figure 16 nucleated inside the sample or was due to a starter weakness, from which rupture propagated, that was located at the surface of the sample. As our measurements are conducted on the sample surface, to answer this question would require coupling our method with additional technology such as acoustic emission or CT scanning. In previous experiments with similar rock materials and conducted under similar conditions, the initial nucleation was observed inside the sample, both with acoustic emission (Benson et al., 2007; Lei et al., 2004; Reches & Lockner, 1994; Salazar Vásquez, Selvadurai, et al., 2022; Thompson et al., 2009) and CT scanning (Higo et al., 2013; McBeck et al., 2019) methods. Also, the evolution of the localized strain in the data (Figure 13a, localizations marked by arrows) is nearly symmetric on the opposite sides of the sample surface, strongly suggesting that the rupture nucleated inside the sample. This is why it is most probable that in the experiment with green Bernese sandstone and confining pressure of 16 MPa (Figures 13–15), the strain localization observed with the optical fiber is an expression of the structure nucleated inside the sample, as the nucleation on the sample surface would have broken the symmetry. Nevertheless, it is possible that in some samples and other conditions, rupture propagation begins on or close to the sample surface. For example, data collected in the uniaxial (unconfined) test with Zimbabwe gabbro exhibits strain localization only on one side of the sample surface (e.g., level 4 in Figure 12a). This indicates fracture development on or near the sample surface.

In addition to the experimental techniques of acoustic emission and CT scanning, inverse modeling based on the obtained fiber optics data could also clarify this question. Confirming this hypothesis means that the developed method provides distributed information regarding the sample damage, which would allow new parameters to be predicted to predict material failure, which is generally limited to the maximum axial differential load. For example, the distributed strain spatial/temporal derivative (as a localization indicator) or the percentage of the sample's surface that is dilating can be easily obtained. To find such a failure predictor requires significant effort, which is outside the scope of the present work.

Section 3 shows that within the sample different behaviors can be observed. This directly impacts the interpretation of triaxial tests. For instance, the importance of dilatancy is enhanced in the numerical modelling of classical

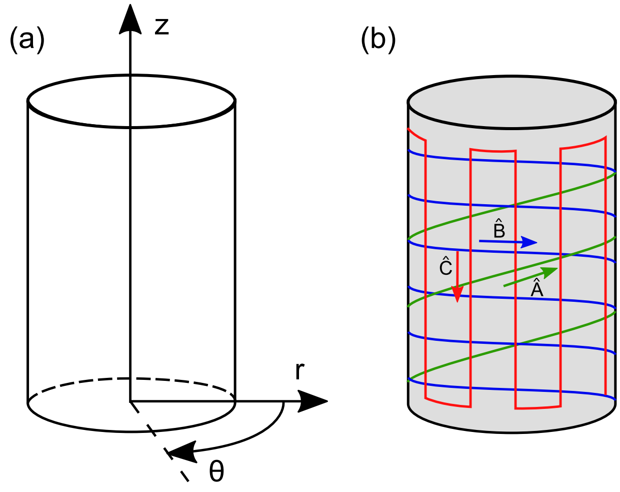

Figure 17. (a) Global coordinate system used in Equations 1 and 2. (b) Diagram of a sample implemented with three fibers with different local orientations ($\hat{A}$, $\hat{B}$, and $\hat{C}$).

rock mechanics post-failure problems (Alejano & Alonso, 2005). The dilatancy angle of the gray Bernese sandstone tested at 6 MPa (Figure 11) is 23.6° considering only the data from the middle of the sample, and increases to 29.4° for the entire sample (24.3% increment). When individual gauges in the distributed data are consider (equivalent to points sensors) the differences are more pronounced. The elatic shear modulus of the Zimbabwe gabbro, calculated from Figure 12b (using a Poisson's ratio of 0.29), is 64 GPa for the gauge with the lowest strain (blue dashed line) and 28.6 GPa in the strain localization (red dashed line). This evidences the large variability in the parameters obtained when using point measurement methods.

The optical fiber method measures the distributed strain in the fiber's core axis direction (shortening or elongation of the core along its axis), which presents a limitation to capturing all the strain tensor components in triaxial tests. Equation

$$\varepsilon_m = [u_r \quad u_\theta \quad u_z] \begin{bmatrix} \varepsilon_{rr} & \varepsilon_{\theta r} & \varepsilon_{zr} \\ \varepsilon_{r\theta} & \varepsilon_{\theta\theta} & \varepsilon_{z\theta} \\ \varepsilon_{rz} & \varepsilon_{\theta z} & \varepsilon_{zz} \end{bmatrix} \begin{bmatrix} u_r \\ u_\theta \\ u_z \end{bmatrix}, \tag{1}$$

defines the strain measured (ε_m), which is the projection of the strain tensor in global coordinates (Figure 17a) into an arbitrary fiber's direction ($\hat{u}$). On the sample's surface, the fiber orientation can only have circumferential (u_θ) and vertical (u_z) components; drilling into the sample is required in order to have a radial component (u_r). Commonly, unaltered samples are required, having a null radial component in the fiber orientation ($u_r = 0$). This implies that all radial components of the strain tensor (ε_{rr}, $\varepsilon_{\theta r}$, and ε_{zr}) cancel out from the measured strain (ε_m) in the projection of Equation 1. The implementation of three arbitrary and different fiber directors, shown in Figure 17b is sufficient to measure the remaining components of the tensor (ε_{zz}, $\varepsilon_{\theta\theta}$, and $\varepsilon_{\theta z}$). Equation

$$\begin{bmatrix} \varepsilon_{\theta\theta} \\ \varepsilon_{\theta z} \\ \varepsilon_{zz} \end{bmatrix} = \begin{bmatrix} u_{A\theta}^2 & 2u_{A\theta}u_{Az} & u_{Az}^2 \\ u_{B\theta}^2 & 2u_{B\theta}u_{Bz} & u_{Bz}^2 \\ u_{C\theta}^2 & 2u_{C\theta}u_{Cz} & u_{Cz}^2 \end{bmatrix}^{-1} \begin{bmatrix} \varepsilon_A \\ \varepsilon_B \\ \varepsilon_C \end{bmatrix}, \tag{2}$$

rotates the three measurements (ε_A, ε_B, and ε_C) from the local fiber directions ($\hat{A}$, $\hat{B}$, and $\hat{C}$) to global cylindrical coordinates. Uchida et al. (2015) measured the vertical, circumferential, and shear strain (ε_{zz}, $\varepsilon_{\theta\theta}$, and $\varepsilon_{\theta z}$) using three different fibers. Nevertheless, equivalent results can be obtained with the present implementation by using the information from the descending stretches of the circumferential fiber (diagonal segments in Figure 8). This has the advantage of reducing the amount of fiber overlap, which is crucial to minimize light attenuation in confined environments. The point measurement methods have the same limitation as described above, but the developed method has the advantage of collecting distributed information. In particular, the representative volume test assumption enables the calculation of the remaining components of the strain tensor ($\varepsilon_{rr} = \varepsilon_{\theta\theta}$, and $\varepsilon_{r\theta} = \varepsilon_{rz} = \varepsilon_{\theta z} = 0$).

The main limitation of the developed method is that it cannot measure the strain field inside the sample, as the CT scan does. Nevertheless, the optical fiber-based method has two advantages over CT scanning: the higher temporal resolution and the implementation efforts. During the test on the green Bernese sandstone under 16 MPa confinement (Figure 13), 858 measurements were taken without interrupting the testing procedure, which allows the strain localization evolution to be observed. Despite the lack of internal data, the fact that the distributed strain field is measured enables (numerical) inverse analysis to be carried out to obtain the micro fracturing inside the sample. Additionally, implementing the method in existing triaxial devices requires the following steps: (a) Drilling a 1 mm diameter hole into the triaxial cell. (b) After the instrumented sample is placed in position, the fibers are fed through the hole, which can be sealed using a two phase epoxy. Post test, the feed-through should be mechanically or chemically cleaned. The optical fibers feed-though can also be sealed using capillary tubes, following the procedure described by Reinsch et al. (2013).

5. Conclusions

A distributed measurement method for triaxial tests using fiber optics technology is presented in this article. The method was first developed in an unconfined test on a steel sample instrumented with optical fibers and strain gauges. Two fiber coatings were assessed: acrylate and polyimide. In the axial direction, the thicker acrylate coating produced a strain lag distance of about 40 mm, while this distance reduced to approximately 2 mm when using the thinner polyimide fiber. This implies that the acrylate fiber should not be used to measure axial strain on samples shorter than 10 cm in height. Considering the values measured on the surface in the middle of the sample, the difference between the optical fibers is about 2%. In the circumferential direction, the differences between the fiber measurements is lower than 1%, because of the larger frictional forces inherent to this direction and the fact that it is extension in this fiber segment (rather than compression in the axial direction). When compared to the strain gauges, the polyimide fiber measurements show a 1% difference. Nevertheless, the polyimide fiber exhibits excessive light attenuation at high confining pressures (above 80 MPa for polished surfaces). In contrast, the acrylate fiber was successfully implemented in tests with confining pressures up to 200 MPa. In general, implementing the developed distributed method requires selecting the correct optical fiber, taking into consideration such factors as the sample size, confining pressure, coating material, roughness of the surface of the sample and temperature variations.

In a second stage, the developed distributed method was implemented in triaxial tests performed on Central Aare granite, Zimbabwe gabbro, and both gray and green Bernese sandstone samples. Our distributed method allowed the observation of the non-uniform strain field that developed before failure. Strain localizations with exponential growth were observed at multiple positions on the sample. 3D optical scanning allowed the virtual reproduction of the test, revealing a correlation between the strain concentrations and the macro fracture positions on the surface. The probable cause of the strain localization is fracture nucleation in the sample and its propagation, causing failure. The distributed strain measurement method using optical fibers has the potential to be implemented in existing triaxial tests. The use of this method allows for an improved interpretation of the mechanical parameters of the sample and data collection to further investigate the failure process.

Appendix A: Rayleigh Scattering Based Distributed Strain Measurements

Optical fibers, as depicted in Figure 1, were first developed in the 1970's for telecommunication (Domingues & Ayman, 2017). They are comprised of an inner cylindrical core, surrounded by two layers: cladding and coating. The cladding is tuned with a lower refractive index to decrease the critical incidence angle, assuring the light beam's confinement within the core. The coating improves the mechanical properties of the cable, protecting it from physical damage. The measurement method starts by launching a light beam into the fiber core from a linear variable frequency laser. Due to small-scale imperfections in the core, random permittivity variations cause the Rayleigh scattering of the light, back reflecting in a random but stable pattern (Froggatt & Moore, 1998).

Figure A1 shows the steps of the OBR system to calculate the distributed strain, where the black arrows indicate the work flow. The backscattered spectrum, shown in Figure A1a, is registered using of a Mach-Zehnder interferometer (Kreger et al., 2016), and projected into the space domain with the inverse fast Fourier transform (1. IFFT; Figure A1b). A spatial window or gauge length is selected (indicated with the black square) and a Fourier Transform (2. FFT) is used to calculate the spectra of this subset (Figure A1c). These random spectra are unique for each fiber section and remain stable as long as the measurements are taken without altering the external conditions. The method compares two measurements to obtain the strain variation (reference measurement in blue and the second measurement in black). Temperature (ΔT) and strain ($\Delta\varepsilon$) variations on the fiber alter the refractive index of the core, causing a frequency shift of the random pattern (Figure A1c). The spectrum shift (Δf) can be related to imposed temperature and strain variations using equation

$$\Delta f = C_{\varepsilon} \cdot (\varepsilon - \varepsilon_0) + C_T \cdot (T - T_0)\,. \tag{A1}$$

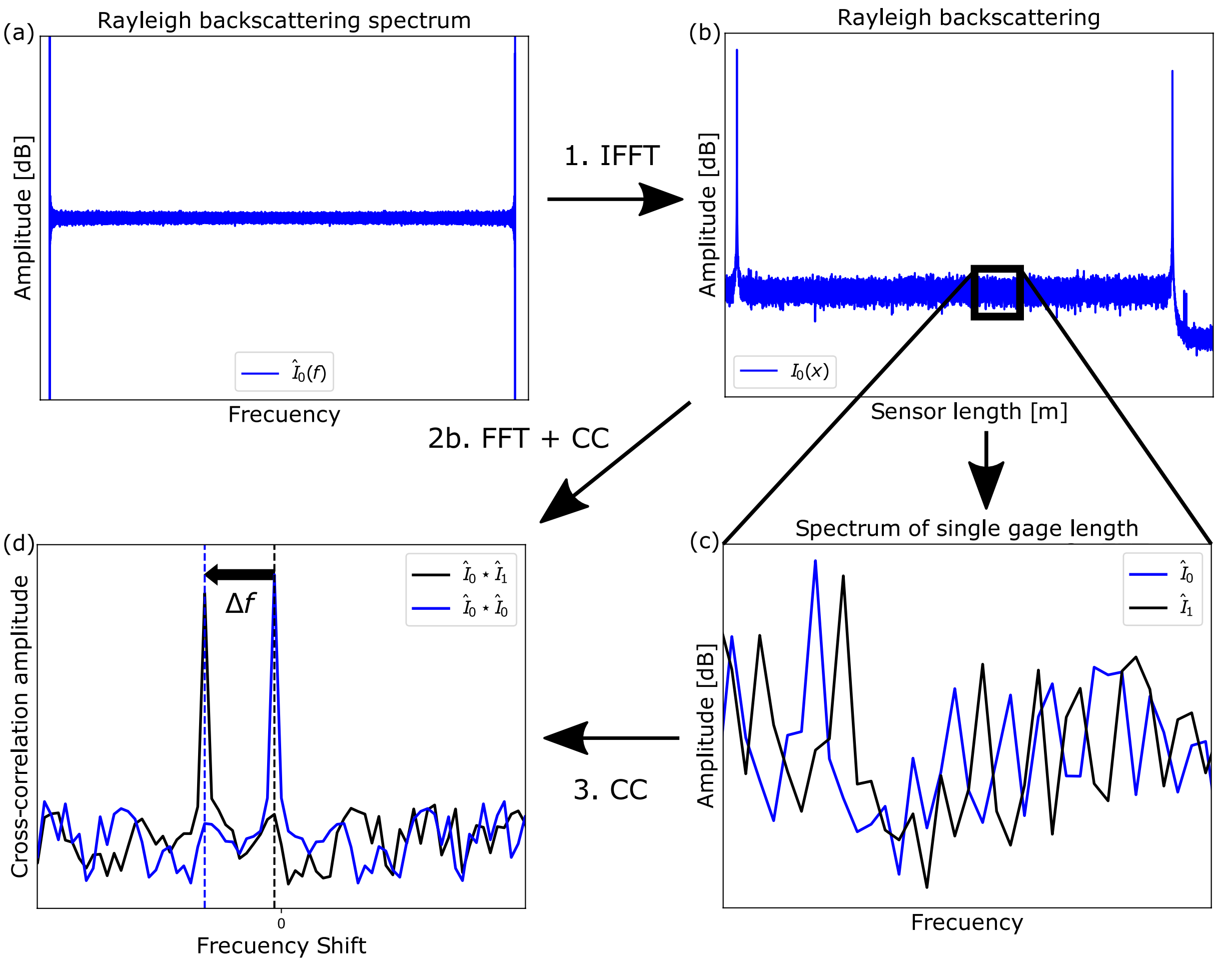

Figure A1. Optical Backscatter reflectometer (OBR) strain calculation process. Arrows indicating calculation steps and work flow. (a) Measured Rayleigh backscatter spectrum. (b) Rayleigh backscatter in time/distance domain. (c) Selected gauge spectrum. (d) Cross-correlation (CC) of reference (blue) and second measurements (black).

It is computationally and visually complicated to recognize the frequency shift (Froggatt & Moore, 1998); therefore, a cross-correlation (3. CC) operation between the reference and strained measurement is performed (Figure A1d). Fourier-transform properties allow merging the two previous calculations (steps 2. and 3.) into a single operation (step 2b).

The cross correlation quality can be affected when the spectral shift between analyzed measurements is large due to the light attenuation or other changes in the spectral pattern. This is usually observed as spikes or noise in the distributed strain that correlate with the position of large strains (i.e., fractures). To avoid this issue, two adaptations were made in our tests. (a) A Python script was developed to automatize the measurements and to increase the sampling rate. (b) Our post-prcessing procedure measures strain increment per time step (i.e., effectively, strain rate). The resulting strain was calculated by integrating the strain rate in a cumulative process as follows. Consecutive measurements were used to calculate the spectral shift (if measurement i was analyzed the reference was measurement $i - 1$), and the strain increment was added. Both adaptations improved the cross correlation by reducing the spectral shift between the analyzed measurements. The chosen post-processing procedure is corroborated by two observations. First, the strain measured on the sample from the cumulative process was compared to the usual method (using a fixed reference measurement); at different stages of the test, the differences are $<1\%$. Second, the strain measured in the segments not attached to the sample (inside and outside the pressure cell) remains below the method resolution.

The equation

$$L_{res} \approx \frac{\lambda^2}{4n\Delta\lambda} \tag{A2}$$

shows the spatial resolution of the method, which depends only on the wave length range of the light beam used to interrogate the fiber (Froggatt & Moore, 1998). L_{res} is the spatial resolution, λ is the free-space wavelength, n is the refractive index of the core, and $\Delta\lambda$ is half of the total range of the change in wavelength. For the data acquired in this work, a center wavelength of 1550 nm and a wavelength range of 21 nm was used, being theoretically possible to reach a spatial resolution in the order of 10^{-5} m. Nevertheless, a decrease in the spatial resolution (due to a shorter gauge length) entails a degradation in the strain resolution (Froggatt & Moore, 1998). In other words, higher spatial resolutions result in higher strain error. In our experience, when a millimetre spatial resolution (2–5 mm) is used, the strain resolution is within the $\pm 5\ \mu\varepsilon$ range.

Appendix B: Triaxial System Setup

The triaxial system used in this work is located at the Eastern Switzerland University of Applied Sciences, and is shown in Figure B1. The system was developed to study the mechanical response of rock materials loaded under confining pressures up to 200 MPa, using oil to conduct pressure. An external heating jacket applies temperatures up to 200°C. The reaction frame consists of steel walls with a thickness of 14 cm. The triaxial cell can accommodate cylindrical samples with a maximum diameter of 7 and 14 cm height.

The axial load is applied from a lower hydraulic piston, with a maximum force of 20 MN (i.e., 5.3 GPa for the sample diameter of 7 cm). When low forces are required, a load cell of 5 MN capacity is placed on the upper reaction plate, with a precision better than 0.05% of the full scale. The displacement load is controlled with a servo-control system. In between the upper reaction piston and the sample, a spherical seat is placed to compensate for nonparallel sample ends (Figures B1, B2c, and B2d). The deformation of the sample is measured with distributed optical fibers and up to four strain gauges.

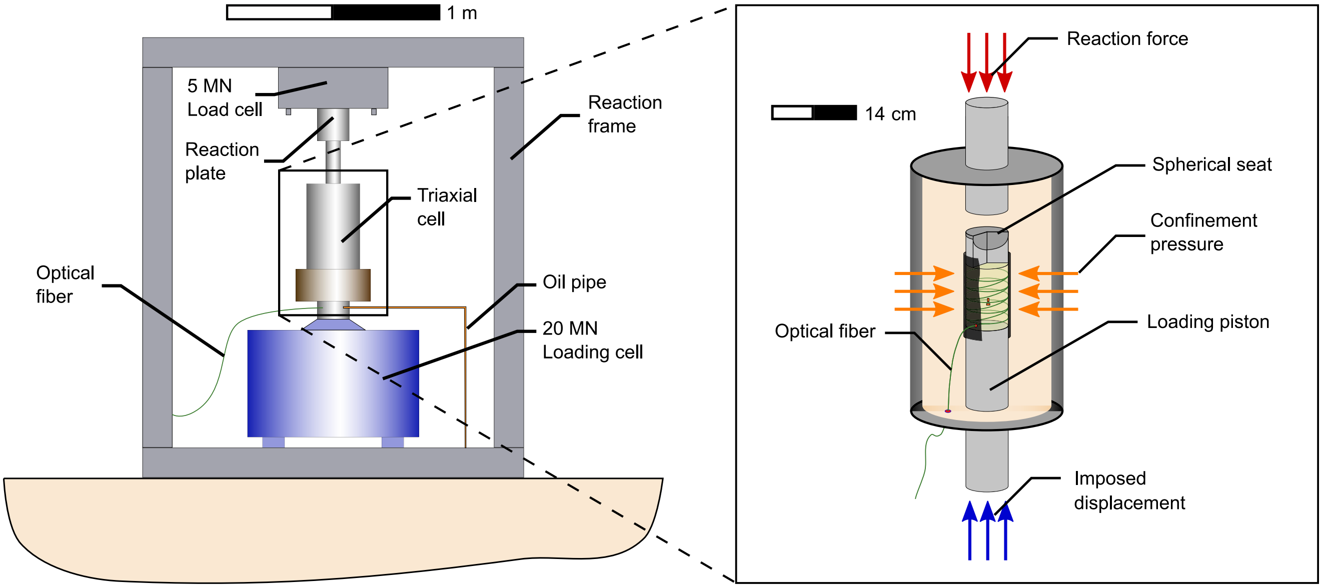

Figure B1. Schematics of the triaxial testing system. The axial load is applied by the bottom piston, and the reaction force is measured by the upper load cell. Sample deformation is measured with optical fibers and strain gauges attached to the sample surface.

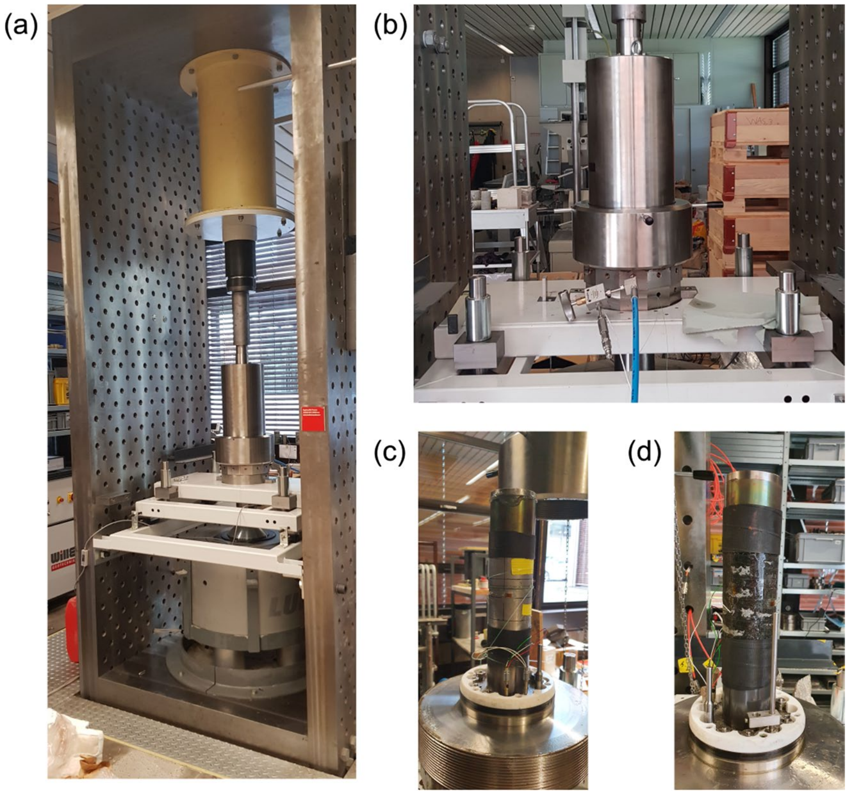

Figure B2. Photographs of the triaxial system and two samples prepared for testing. (a) Triaxial sytem and reaction frame. (b) Triaxial cell with the optical fiber and oil feed-though. (c) Steel sample implemented with optical fiber and strain gauges (results given in Section 2.3). (d) Zimbabwe gabbro sample ready for uniaxial testing (Figure 12).

Appendix C: Light Attenuation and Pressure Sensitivity

Figure C1 shows the distributed light intensity of the back reflected signal, during the isotropic confinement stage of the triaxial tests. No corrections are applied to the data. The polyimide fiber was used on a steel sample (Figure C1a), while the acrylate fiber was installed on a granite sample (Figure C1b). The acrylate fiber was

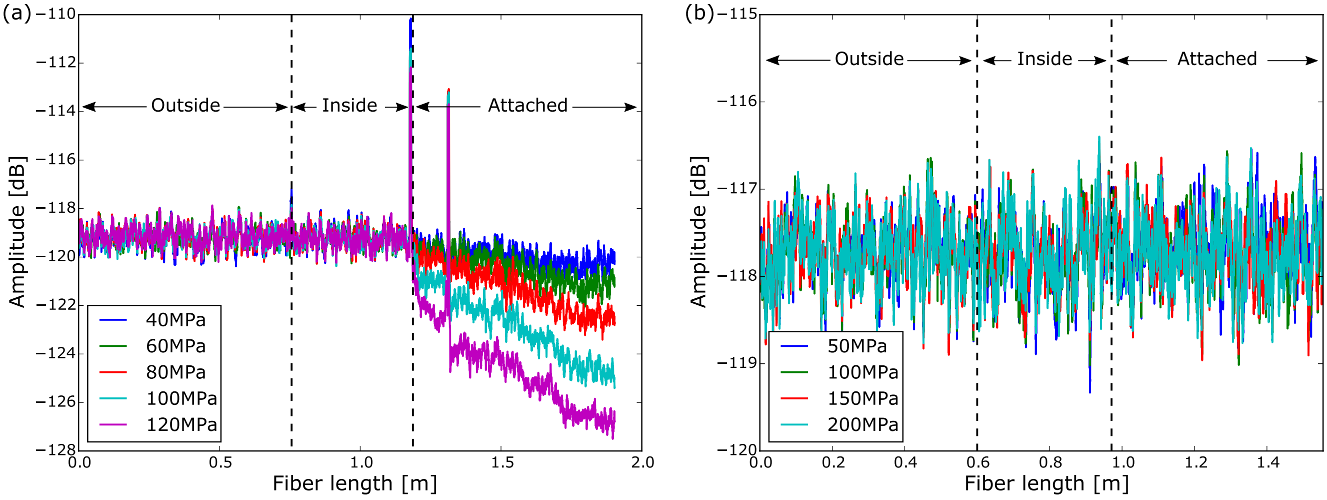

Figure C1. Distributed light intensity of the back reflected signal. Samples subjected to increasing isotropic confinements. Three fiber segments are marked: outside the triaxial cell, inside but loose in the oil and attached to the sample. (a) Steel sample implemented with polyimide fiber. (b) Central Aare granite sample implemented with acrylate fiber.

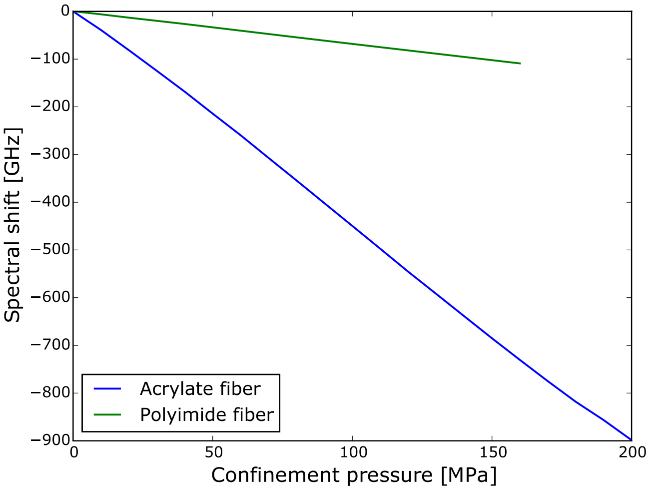

Figure C2. Average spectral shift on the loose segment of the optical fibers (Figure C1).

implemented on the granite sample because of the unfavorable surface roughness conditions. Three fiber segments are marked in the plots: The first corresponds to the stretch outside the triaxial cell (unconfined), followed by the section after feed through (free in the oil), and the segment glued to the sample. Light attenuation is visible in the attached segment of the polyimide fiber, which increases with pressure (Figure C1a). Strain measurements were feasible up to attenuation of 2 dB, failing under pressures above 80 MPa. The thicker acrylate coating diminishes light attenuation, measuring the distributed strain under pressures of 200 MPa (Figure C1b).

The pressure sensitivity of the optical fibers are shown in Figure C2. The average spectral shift was calculated from the free segment inside the cell ("Inside" segments in Figure C1a and C1b). This information was not used to compensate the distributed measurements in this work, but are given to give evidence of the pressure sensitivity of the fibers. The acrylate fiber is about 6.5 times more sensitive to pressure than the polyimide, presumably because of its larger diameter and coating mechanical properties. With this configuration, the pressure accuracy is approximately 0.3 MPa for the acrylate fiber, while for the polyimide it is about 2 MPa.

Appendix D: Additional Tests

The results of a gabbro sample tested at 10 MPa confining pressure is shown in Figure D1. The strain localization was evident at level C5 at 0 cm in the perimeter, and propagated to the level C4 at the same position. On average (Figure D1b), the upper and lower levels show the largest circumferential strain, which is lowest in the middle segment. This is contrary to expectations because frictional forces at the loading plate interfaces should restrict the sample deformation.

The results for a green Bernese sandstone sample tested under unconfined (uniaxial) conditions are shown in Figure D2. Two strain localizations are indicated, separated in level C5 and merging at level C1 (Figure D2a). The dip angle of the fracture surfaces are sub-vertical, correlating with the strain localization.

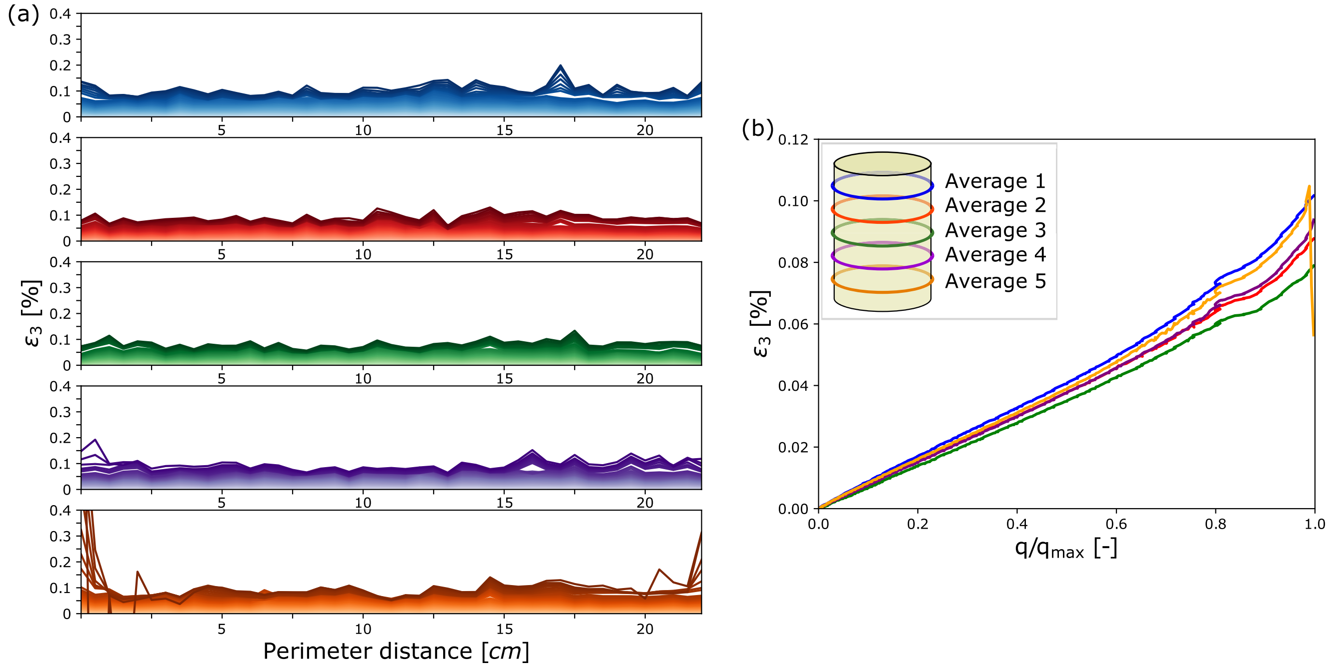

Figure D1. Zimbabwe gabbro tested under 10 MPa of confining pressure. (a) Circumferential distributed strain measurements at each of the levels (Figure 8b). Color intensity marks the loading increment. (b) Circumferential strain development with normalized differential stress ($q = \sigma_1 – \sigma_3$). The average for each level is compared.

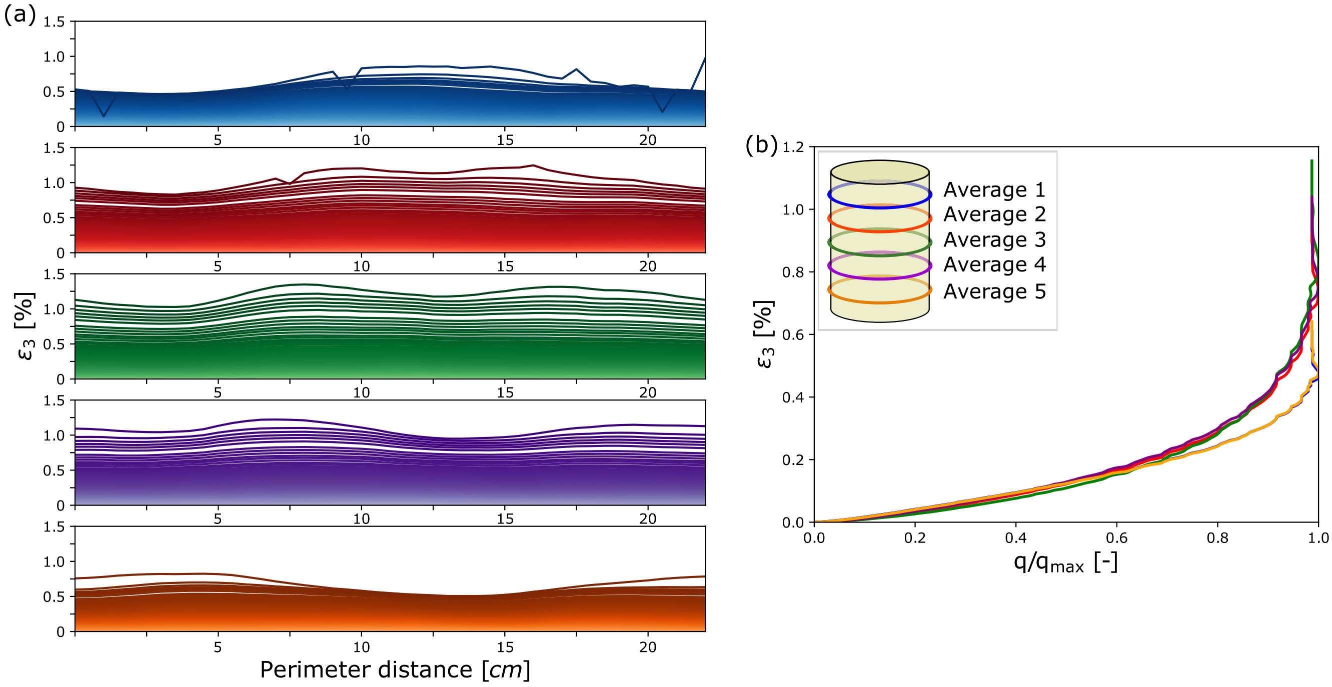

Figure D2. Green Bernese sandstone tested under unconfined (uniaxial) conditions. (a) Circumferential distributed strain measurements at each of the levels (Figure 8b). Color intensity marks the loading increment. (b) Strain development average per level. Circumferential strain development with normalized differential stress ($q = \sigma_1 – \sigma_3$). The average of each level is compared.

Appendix E: Distributed Strain Measurement Method Assessment Under Confined Conditions

Figure E1 compares the measurements obtained with the strain gauges and the acrylate-coated optical fiber from the test performed on the green Bernese sandstone, Figure 13. Pre-peak, the maximum strain difference between technologies is approximately 120 $\mu\varepsilon$, which corresponds to 2.89% error. Post-peak the maximum error increases to 4.93%. The average difference during the test was 2.64%.

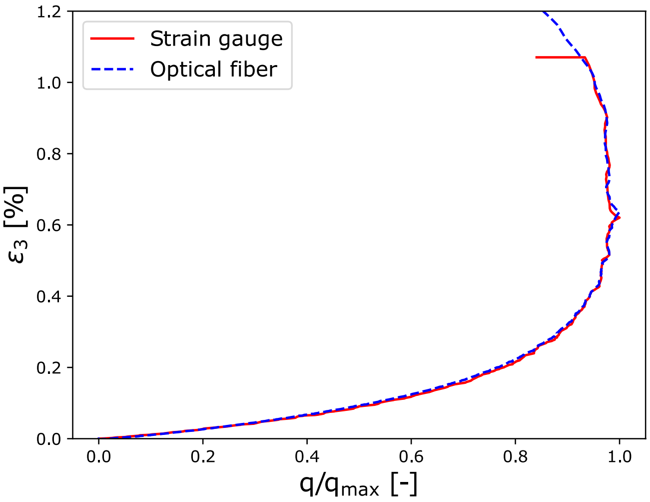

Figure E1. Green Bernese sandstone tested under 16 MP confining pressure. The circumferential strain measured using the optical fiber and strain gauge are compared.

Data Availability Statement

Data Availability Statement All the experimental data presented in this manuscript have been obtained in this work and is available in Zenodo repository (Salazar Vásquez, Rabaiotti, et al., 2022).

Acknowledgments

We thank Massimo Facchini (Iridis Solutions GmbH) for his help in selecting suitable optical fibers and Hansruedi Schneider for the initial development of the triaxial loading system used in this work. We are also grateful to Lui Dong and Brice Lecampion for providing the Zimbabwe gabbro and to Marti AG for supplying the gray and green Bernese sandstones used in this research. We are indebted to Paul Hardegger for important discussions and advice that helped to complete this work. Last but not least, we appreciate the detailed and constructive comments of the Editor, Yves Bernabe, and anonymous reviewers that greatly improved the quality of the manuscript. This work was supported by the Swiss Innovation Agency (Innosuisse) as a part of the Swiss Competence Center for Energy Research - Supply of Electricity (SCCER-SoE). LNG is beholden to Larry Murdoch, Scott DeWolf, and Dmitry Garagash for stimulating discussions. He also appreciates partial support of the US Department of Energy (project DE-FE0028292). Open access funding provided by Eidgenossische Technische Hochschule Zurich.

References

Alejano, L., & Alonso, E. (2005). Considerations of the dilatancy angle in rocks and rock masses. *International Journal of Rock Mechanics and Mining Sciences*, *42*(4), 481–507. https://doi.org/10.1016/j.ijrmms.2005.01.003

Alj, I., Quiertant, M., Khadour, A., Grando, Q., Terrade, B., Renaud, J.-C., & Benzarti, K. (2020). Experimental and numerical investigation on the strain response of distributed optical fiber sensors bonded to concrete: Influence of the adhesive stiffness on crack monitoring performance. *Sensors*, *20*(18), 5144. https://doi.org/10.3390/s20185144

Alonso, E., Pinyol, N., & Puzrin, A. (2010). *Geomechanics of failures: Advanced topics* (Vol. 277). Springer.

Ansari, F., & Libo, Y. (1998). Mechanics of bond and interface shear transfer in optical fiber sensors. *Journal of Engineering Mechanics*, *124*(4), 385–394. https://doi.org/10.1061/(ASCE)0733-9399

Bai, M., & Seitz, W. (1994). A fiber optic sensor for water in organic solvents based on polymer swelling. *Talanta*, *41*(6), 993–999. https://doi.org/10.1016/0039-9140(94)E0049-W

Bassil, A., Chapeleau, X., Leduc, D., & Abraham, O. (2020). Concrete crack monitoring using a novel strain transfer model for distributed fiber optics sensors. *Sensors*, *20*(8), 2220. https://doi.org/10.3390/s20082220

Benson, P., Thompson, B., Meredith, P., Vinciguerra, S., & Young, P. (2007). Imaging slow failure in triaxially deformed Etna basalt using 3D acoustic-emission location and X-ray computed tomography. *Geophysical Research Letters*, *34*(3), L03303. https://doi.org/10.1029/2006GL028721

Bernard, P. (2001). From the search of 'precursors' to the research on 'crustal transients'. *Tectonophysics*, *338*(3), 225–232. https://doi.org/10.1016/S0040-1951(01)00078-6

Billon, A., Hénault, J.-M., Quiertant, M., Taillade, F., Khadour, A., Martin, R.-P., & Benzarti, K. (2015). Qualification of a distributed optical fiber sensor bonded to the surface of a concrete structure: A methodology to obtain quantitative strain measurements. *Smart Materials and Structures*, *24*(11), 115001. https://doi.org/10.1088/0964-1726/24/11/115001

Bobet, A. (2000). The initiation of secondary cracks in compression. *Engineering Fracture Mechanics*, *66*(2), 187–219. https://doi.org/10.1016/S0013-7944(00)00009-6

Bohnhoff, M., Martínez-Garzón, P., Bulut, F., Stierle, E., & Ben-Zion, Y. (2016). Maximum earthquake magnitudes along different sections of the North Anatolian fault zone. *Tectonophysics*, *674*, 147–165. https://doi.org/10.1016/j.tecto.2016.02.028

Cornet, F. H., Helm, J., Poitrenaud, H., & Etchecopar, A. (1998). Seismic and aseismic slips induced by large-scale fluid injections. In S. Talebi (Ed.), *Seismicity associated with mines, reservoirs and fluid injections* (pp. 563–583). Birkhäuser Basel.

Crameri, T., Höttges, A., & Rabaiotti, C. (2019). Distributed fiber optics monitoring of the Lago Bianco dam in Switzerland. Assessment and rehabilitation of civil structures. 5th International Conference on Smart Monitoring, Assessment and Rehabilitation of Civil Structures, Postdam, Germany.

Davis, R. O., & Selvadurai, A. P. S. (2005). *Plasticity and geomechanics*. Cambridge University Press.

Domede, N., Parent, T., & Sellier, A. (2019). Mechanical behaviour of granite: A compilation, analysis and correlation of data from around the world. *European Journal of Environmental and Civil Engineering*, *23*(2), 193–211. https://doi.org/10.1080/19648189.2016.1275984

Domingues, M., & Ayman, R. (2017). *Optical fiber sensors for lot and smart devices*. Springer.

Durand, V., Martínez-Garzón, P., Gualandi, A., Haghighi, M., Motagh, M., Dresen, G., & Bohnhoff, M. (2021). Deciphering deformation along submarine fault branches below the eastern Sea of Marmara (Turkey): Insights from seismicity, strainmeter, GPS and InSAR data. In *Egu general assembly conference abstracts* (p. EGU21-8651). https://doi.org/10.5194/egusphere-egu21-8651

Falcetelli, F., Rossi, L., Di Sante, R., & Bolognini, G. (2020). Strain transfer in surface-bonded optical fiber sensors. *Sensors*, *20*(11), 3100. https://doi.org/10.3390/s20113100

Froggatt, M., & Moore, J. (1998). High-spatial-resolution distributed strain measurement in optical fiber with Rayleigh scatter. *Applied Optics*, *37*(10), 1735–1740. https://doi.org/10.1364/AO.37.001735

Germanovich, L. N., Salganik, R. L., Dyskin, A. V., & Lee, K. K. (1994). Mechanisms of brittle fracture of rock with pre-existing cracks in compression. *Pure and Applied Geophysics*, *143*(1), 117–149. https://doi.org/10.1007/BF00874326

Hauswirth, D. (2015). *A study of the novel approaches to soil displacement monitoring using distributed fiber optic strain sensing (Unpublished doctoral dissertation)*. ETH Zurich.

Hauswirth, D., Puzrin, A., Carrera, A., Standing, J., & Wan, M. (2014). Use of fibre-optic sensors for simple assessment of ground surface displacements during tunnelling. *Géotechnique*, *64*(10), 837–842. https://doi.org/10.1680/geot.14.T.009

Higo, Y., Oka, F., Sato, T., Matsushima, Y., & Kimoto, S. (2013). Investigation of localized deformation in partially saturated sand under triaxial compression using microfocus X-ray CT with digital image correlation. *Soils and Foundations*, *53*(2), 181–198. https://doi.org/10.1016/j.sandf.2013.02.001

Inaudi, D., & Glisic, B. (2005). Application of distributed fiber optic sensory for SHM. *Proceedings of the ISHMII-2*, *1*, 163–169.

Jaeger, Cook, N., & Zimmerman, R. (2007). *Fundamentals of rock mechanics*. John Wiley & Sons.

Janting, J., Pedersen, J. K. M., Woyessa, G., Nielsen, K., & Bang, O. (2019). Small and robust all-polymer fiber Bragg grating based pH sensor. *Journal of Lightwave Technology*, *37*(18), 4480–4486. Retrieved from http://opg.optica.org/jlt/abstract.cfm?URI=jlt-37-18-4480

Karev, V., Kovalenko, Y., & Ustinov, K. (2020). *Geomechanics of oil and gas wells*. Springer.

Katz, O., & Reches, Z. (2004). Microfracturing, damage, and failure of brittle granites. *Journal of Geophysical Research*, *109*(B1). https://doi.org/10.1029/2002JB001961

Kellerhals, P., Haefeli, C., & Staeger, D. (2005). 1166 Bern - Geologischen Atlas Schweiz 1:25000, Karte 100. ISBN 3-906723-63-1.

Khanikar, T., & Singh, V. K. (2021). *Gelatin coated optical fiber probe as a pH sensor: An experimental analysis*. In K. Singh, A. K. Gupta, S. Khare, N. Dixit, & K. Pant (Eds.), ICOL-2019 (pp. 189–192). Springer.

Kovalyshen, Y., Banks, S., & Giwelli, A. (2018). Measurement of rock strain using fiber bragg grating sensors (Vol. All Days). (ARMA-2018-831)

Kreger, S. T., Rahim, N. A. A., Garg, N., Klute, S. M., Metrey, D. R., Beaty, N., et al. (2016). Optical frequency domain reflectometry: Principles and applications in fiber optic sensing. In E. Udd, G. Pickrell, & H. H. Du (Eds.) *Fiber optic sensors and applications XIII* (Vol. 9852, pp. 218–227). SPIE. https://doi.org/10.1117/12.2229057

Kündig, R., Mumenthaler, T., Eckhardt, P., Keusen, H., Schindler, C., Hofmann, F., et al. (1997). *Die mineralischen rohstoffe der schweiz*. Schweizerische Geotechnische Kommission.

Labhart, T., Schwizer, B., Gisler, C., & Renner, F. (2015). 1211 Meiental, mit Südostteil von Blatt 1191 Engelberg. - Geological Atlas Schweiz 1:25000, Karte 146. ISBN 3-906723-31.

Lei, X., Masuda, K., Nishizawa, O., Jouniaux, L., Liu, L., Ma, W., et al. (2004). Detailed analysis of acoustic-emission activity during catastrophic fracture of faults in rock. *Journal of Structural Geology*, *26*(2), 247–258. https://doi.org/10.1016/S0191-8141(03)00095-6

Li, H., Zhao, J., & Li, T. (1999). Triaxial compression tests on a granite at different strain rates and confining pressures. *International Journal of Rock Mechanics and Mining Sciences*, *36*(8), 1057–1063. https://doi.org/10.1016/s1365-1609(99)00120-3

Liu, D. (2021). Hydraulic fracture growth in quasi-brittle materials. (p. 236). https://doi.org/10.5075/epfl-thesis-8360

Martínez-Garzón, P., Durand, V., Bentz, S., Turkmen, T., Kwiatek, G., Dresen, G., et al. (2021). Near-fault seismic monitoring reveals the long-lasting activation of a local fault in the Marmara region controlled by slow slip. In *EGU general assembly conference abstracts*. (p. EGU21-7710). https://doi.org/10.5194/egusphere-egu21-7710

Materials Hub, E. (2017). Marterial archiv. Retrieved from https://materialarchiv.ch

McBeck, J. A., Cordonnier, B., Vinciguerra, S., & Renard, F. (2019). Volumetric and shear strain localization in Mt. Etna basalt. *Geophysical Research Letters*, *46*(5), 2425–2433. https://doi.org/10.1029/2018GL081299

McCurley, M. F., & Seitz, W. (1991). Fiber-optic sensor for salt concentration based on polymer swelling coupled to optical displacement. *Analytica Chimica Acta*, *249*(2), 373–380. https://doi.org/10.1016/S0003-2670(00)83009-3

Minardo, A., Bernini, R., Amato, L., & Zeni, L. (2012). Bridge monitoring using brillouin fiber-optic sensors. *IEEE Sensors Journal*, *12*(1), 145–150. https://doi.org/10.1109/jsen.2011.2141985

Moffat, R., Sotomayor, J., & Beltrán, J. F. (2015). Estimating tunnel wall displacements using a simple sensor based on a brillouin optical time domain reflectometer apparatus. *International Journal of Rock Mechanics and Mining Sciences*, *75*, 233–243. https://doi.org/10.1016/j.ijrmms.2014.10.013

Nadai, A. (1963). *Theory of flow and fracture of solids* (Vol. 2). McGraw-Hill Book Company Incorporated. pp. 705.

Puzrin, A. (2012). *Constitutive modelling in geomechanics: Introduction*. Springer Science & Business Media.

Puzrin, A., Alonso, E., & Pinyol, N. (2010). *Geomechanics of failures*. Springer.

Rabaiotti, C., & Malecki, C. (2018). In situ testing of barrette foundations for a high retaining wall in molasse rock. *Géotechnique*, *68*(12), 1056–1070. https://doi.org/10.1680/jgeot.17.P.144

Reches, Z., & Lockner, D. A. (1994). Nucleation and growth of faults in brittle rocks. *Journal of Geophysical Research*, *99*(B9), 18159–18173. https://doi.org/10.1029/94JB00115

Reinsch, T., Cunow, C., Schrötter, J., & Giese, R. (2013). Simple feed-through for coupling optical fibres into high pressure and temperature systems. *Measurement Science and Technology*, *24*(3), 037001. https://doi.org/10.1088/0957-0233/24/3/037001

Salazar Vásquez, A., Rabaiotti, C., Germanovich, L. N., & Puzrin, A. M. (2022). Data set: Distributed fiber optics measurements of rock deformation and failure in triaxial tests. *Zenodo*. https://doi.org/10.5281/zenodo.6837705

Salazar Vásquez, A., Selvadurai, P. A., Niu, Z., Bianchi, P., Rabaiotti, C., Madonna, C., et al. (2022). Insights into triaxial testing using coupled acoustic emission and distributed optical fiber strain measurements. (Paper presented at the 56th U.S. Rock Mechanics/Geomechanics Symposium).

Schmidt-Hattenberger, C., Naumann, M., & Borm, G. (2003). Fiber Bragg grating strain measurements in comparison with additional techniques for rock mechanical testing. *IEEE Sensors Journal*, *3*(1), 50–55. https://doi.org/10.1109/jsen.2003.809025

Scotti, O., & Cornet, F. (1994). In situ evidence for fluid-induced aseismic slip events along fault zones. *International Journal of Rock Mechanics and Mining Sciences & Geomechanics Abstracts*, *31*(4), 347–358. https://doi.org/10.1016/0148-9062(94)90902-4

Sedighi, S., Soto, M. A., Jderu, A., Dorobantu, D., Enachescu, M., & Ziegler, D. (2021). Swelling-based distributed chemical sensing with standard acrylate coated optical fibers. *Sensors*, *21*(3), 718. https://doi.org/10.3390/s21030718

Shakhsher, Z., Seitz, W. R., & Legg, K. D. (1994). Single fiber-optic pH sensor based on changes in reflection accompanying polymer swelling. *Analytical Chemistry*, *66*(10), 1731–1735. https://doi.org/10.1021/ac00082a021

Sieńko, R., Zych, M., Bednarski, Ł., & Howiacki, T. (2019). Strain and crack analysis within concrete members using distributed fibre optic sensors. *Structural Health Monitoring*, *18*(5–6), 1510–1526. https://doi.org/10.1177/1475921718804466

Sun, Y., Li, Q., Yang, D., Fan, C., & Sun, A. (2016). Investigation of the dynamic strain responses of sandstone using multichannel fiber-optic sensor arrays. *Engineering Geology*, *213*, 1–10. https://doi.org/10.1016/j.enggeo.2016.08.008

Tan, X., Bao, Y., Zhang, Q., Nassif, H., & Chen, G. (2021). Strain transfer effect in distributed fiber optic sensors under an arbitrary field. *Automation in Construction*, *124*, 103597. https://doi.org/10.1016/j.autcon.2021.103597

Thompson, B., Young, R., & Lockner, D. (2009). Premonitory acoustic emissions and stick-slip in natural and smooth, faulted westerly granite. *Journal of Geophysical Research*, *114*(B2), B02205. https://doi.org/10.1029/2008JB005753

Uchida, S., Levenberg, E., & Klar, A. (2015). On-specimen strain measurement with fiber optic distributed sensing. *Measurement*, *60*, 104–113. https://doi.org/10.1016/j.measurement.2014.09.054

Van der Baan, M., & Chorney, D. (2019). Insights from micromechanical modeling of intact rock failure: Event characteristics, stress drops, and force networks. *Journal of Geophysical Research: Solid Earth*, *124*(12), 12955–12980. https://doi.org/10.1029/2019JB018121

Vorster, T. E. B., Soga, K., Mair, R. J., Bennett, P. J., Klar, A., & Choy, C. K. (2006). The use of fibre optic sensors to monitor pipeline response to tunnelling. In *GeoCongress 2006* (pp. 1–6). https://doi.org/10.1061/40803(187)33

Wang, H., & Xiang, P. (2016). Strain transfer analysis of optical fiber based sensors embedded in an asphalt pavement structure. *Measurement Science and Technology*, *27*(7), 075106. https://doi.org/10.1088/0957-0233/27/7/075106

Wang, H., Xiang, P., & Li, X. (2016). Theoretical analysis on strain transfer error of FBG sensors attached on steel structures subjected to fatigue load. *Strain*, *52*(6), 522–530. https://doi.org/10.1111/str.12195

Wang, H., & Zhou, Z. (2014). Advances of strain transfer analysis of optical fibre sensors. *Pacific Science Review*, *16*(1), 8–18. https://doi.org/10.1016/j.pscr.2014.08.002

Xu, J., Dong, Y., Zhang, Z., Li, S., He, S., & Li, H. (2016). Full scale strain monitoring of a suspension bridge using high performance distributed fiber optic sensors. *Measurement Science and Technology*, *27*(12), 124017. https://doi.org/10.1088/0957-0233/27/12/124017

Yabesh, G., da Silva Falcão, B., Giwelli, A., Nogueira Kiewiet, M., Kiewiet, L., Esteban, L., et al. (2021). Can FBG sensors measure rock deformation under hydrostatic pressure? (Vol. All Days). (ARMA-IGS-21-074).

Yang, Y., Bhalla, S., Wang, C., Soh, C., & Zhao, J. (2007). Monitoring of rocks using smart sensors. *Tunnelling and Underground Space Technology*, *22*(2), 206–221. https://doi.org/10.1016/j.tust.2006.04.004

Zhang, C., Shi, B., Zhu, H. H., Wang, B. J., & Wei, G. Q. (2020). Toward distributed fiber-optic sensing of subsurface deformation: A theoretical quantification of ground-borehole-cable interaction. *Journal of Geophysical Research: Solid Earth*, *125*(3), e2019JB018878. https://doi.org/10.1029/2019JB018878

Zhang, S., Liu, H., Cheng, J., & De Jong, M. J. (2020). A mechanical model to interpret distributed fiber optic strain measurement at displacement discontinuities. *Structural Health Monitoring*. https://doi.org/10.1177/1475921720964183

Zheng, X., Shi, B., Zhang, C.-C., Sun, Y., Zhang, L., & Han, H. (2021). Strain transfer mechanism in surface-bonded distributed fiber-optic sensors subjected to linear strain gradients: Theoretical modeling and experimental validation. *Measurement*, *179*, 109510. https://doi.org/10.1016/j.measurement.2021.109510